IEEE Journal of Microwaves

Received 7 November 2022; revised 15 February 2023; accepted 4 March 2023. Date of publication 20 March 2023; date of current version 7 April 2023.

Digital Object Identifier 10.1109/JMW.2023.3254135

The Impact of Antenna Array Calibration Errors on MIMO and Multi-Channel Synthetic Aperture Radar Imaging

JOHANNA GEISS (Student Member, IEEE), ERIK SIPPEL, MICHAEL BRAUNWARTH, AND MARTIN VOSSIEK (Fellow, IEEE)

(Regular Paper)

Institute of Microwaves and Photonics, Friedrich-Alexander-Universität Erlangen-Nürnberg, 91058 Erlangen, Germany

CORRESPONDING AUTHOR: Johanna Geiss (e-mail: johanna.geiss@fau.de).

This work was supported by Deutsche Forschungsgemeinschaft (DFG, German Research Foundation) under Grants VO 1453/42-1 and GRK 2680 – Project-ID 437847244.

ABSTRACT In radar imaging, any lateral resolution is either attained using antenna arrays or by synthetic aperture radar (SAR) principles. Recently, the combination of both approaches to a multi-channel SAR (MCSAR) has gained increased attention. However, antenna arrays are impaired by unknown calibration errors, particularly phase errors, amplification deviations, mutual coupling, and phase center position deviation of the antenna element. Since, first, established calibration procedures are often non-ideal and, second, the calibration parameters usually vary over time due to aging and changes in temperature, calibration errors distort the measurements during the radar operation. Therefore, current research focuses on finding new practical calibration procedures. However, hardly any research has been conducted to analyze the basic effects which erroneous calibration parameters have on the reconstructed image in MCSAR or MIMO radar. In this work, we analyze the effects of multiple calibration error types on MCSAR and MIMO radar imaging. Both measurement principles lead to periodic error patterns, resulting in deterministic distortions. The derived relations can be used to precisely predict the position and number of ghost targets caused by calibration errors for known measurement setups and targets. For this, no information about the actual calibration errors is required. Furthermore, worst-case distortion levels are provided for different bounded errors allowing rough estimates of the impact of different error types on the image's distortion level. The findings are validated via measurements using a 76 GHz FMCW MIMO radar.

INDEX TERMS Antenna array, automotive radar, calibration errors, ghost targets, radar, SAR.

I. INTRODUCTION

Today, imaging radar sensors are used in many applications ranging from remote sensing [1], [2], [3] over non-destructive testing [4] and security scanning [5] to the broad area of automotive radar [6], [7], [8]. Generally, imaging radar collects cross-range information by utilizing either antenna arrays in a single-input multiple-output (SIMO) or multiple-input multiple-output (MIMO) manner [9], [10], or by moving a single antenna to create a synthetic aperture radar (SAR) [2], [11]. The combination of both approaches, i.e., moving complete antenna arrays, leads to the principle of multi-channel SAR (MCSAR), either implemented as SIMO-SAR or MIMO-SAR. MCSAR has been investigated primarily in remote sensing to further increase the imaging resolution and relax the demand on the pulse repetition frequency (PRF) [3], [12], [13], [14]. In the automotive radar field, the MIMO concept is established to create large apertures with limited sensor size. In contrast, SAR imaging is a topic that has only emerged in the past years but has gained increasing interest because of its high-resolution possibilities [7], [8], [15], [16], [17], [18]. Especially for radars with a side-looking arrangement, the car's movement can be exploited to directly

apply the SAR principle. While most of this research focuses on single antenna SAR for now, the extension to MCSAR is a logical next step, which has already been investigated in e.g. [19], [20], because most automotive radars are already equipped with MIMO antenna arrays.

When using antenna arrays, the imaging performance is generally deteriorated due to mismatches between the channels caused by gain and phase errors, shifted antenna phase centers, and mutual coupling between the antennas [21]. Therefore, antenna arrays should be calibrated to eliminate or reduce these effects. Calibration procedures usually require measurements to targets at known positions in a multipath-free far-field environment, such as an anechoic chamber [22], [23], [24]. Using elaborated approaches, as in [25], [26], allows to reduce the high requirements on the calibration setup. Nevertheless, radar sensors, especially in the automotive sector, typically suffer from some residual calibration error because no sufficiently frequent recalibration is performed to maintain high imaging quality [27]. As reported in e.g. [28], [29], [30], such remaining mismatches between the antennas in a MCSAR setting and even in single MIMO measurements lead to replicas in the radar image, generally referred to as ghost targets, because channel specific errors are repeated over the full aperture. To provide a visual intuition on the examined research content of this paper, this creation of ghost targets is illustrated in Fig. 1. Here, a SIMO-SAR measurement using a 76 GHz frequency-modulated continuous-wave (FMCW) MIMO-radar with 8 receive channels was performed to an automotive target scene shown in Fig. 1(b). The MIMO array is shown in Fig. 1(a). For the SIMO-SAR measurement, only the leftmost TX antenna was used. The measurement was performed such that a synthetic aperture of the length 12 cm was sampled uniformly. Then, radar images were reconstructed via backprojection [31]. First, the calibration data found via the offline calibration proposed in [25] was used and second, additional phase errors of $\pm 20^\circ$ were added to the individual channels during the reconstruction. The resulting images are shown in Figure 1(c) and 1(d), respectively. While the scene in Fig. 1(b) is well reconstructed in Fig. 1(c), the radar image in Fig. 1(d) is strongly degraded via numerous ghost targets. These ghost targets occur as replicas of the true targets within regular distances, thereby, forming distinct patterns. Such artifacts within the radar image, which can also be caused by multipath or interference, are a relevant safety issue in autonomous driving. Therefore, on the one hand, the identification and reduction of these ghost targets is subject of current research [32], [33]. On the other hand, there is a need to detect occurring errors in the calibration, which can be caused by aging, temperature change, and deformation, to initiate re-calibration of the sensor [34]. Nonetheless, only little research has been conducted to analytically investigate the effects of calibration errors on MCSAR radar imaging and the corresponding creation of ghost targets. In [35], the authors discuss the impact of phase and amplitude errors on the radar image's ambiguity level in the radar image without discussing the ghost target positions. [30] exemplarily shows this relation

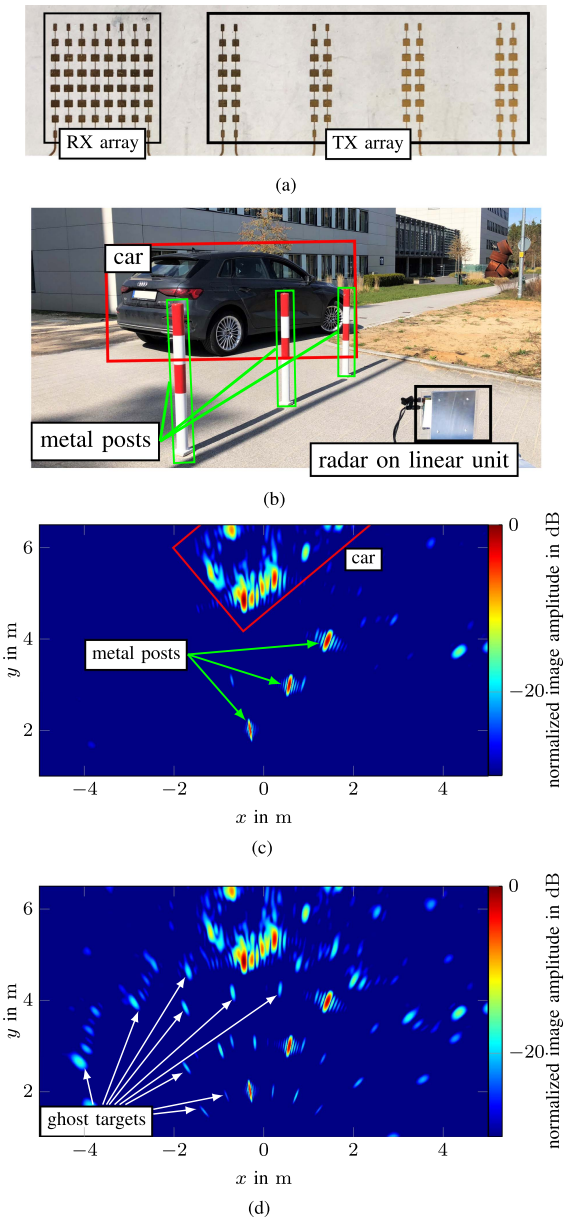

FIGURE 1. Example of a SIMO-SAR radar measurement to an automotive target scene shown in (b) using the antenna array shown in (a). The measurements were reconstructed using ideal calibration in (c) and with phase errors in (d). (a) Antenna array of the used 76 GHz FMCW MIMO radar. Only the leftmost TX antenna was used to simulate a SIMO radar. (b) Automotive target scene comprising a car and three metal posts with the radar on a linear unit, which provides the movement to create the synthetic aperture. (c) Reconstructed SIMO-SAR radar image using a calibrated radar. (d) Reconstructed SIMO-SAR radar image with phase errors of ±20° added to the channels. Exemplary ghost targets caused by the calibration errors are indicated via white arrows.

for a two antenna array but not forarbitrary arrays arrays. Furthermore, neither [35] nor [30] discuss the influence of mutual coupling, which is relevant in most automotive radar sensors using closely spaced antennas either in the receiver (RX) or the transmitter (TX) array.

In MIMO radars, a virtual aperture is created by the convolution of the RX and TX subarrays [36]. They are often

realized as uniform linear arrays (ULAs), leading to a periodic evaluation of the repeated subarray during the formation of the virtual aperture. In most scenarios of SAR measurements, including automotive applications, a constant position shift of the radar between consecutive measurements is assumed due to a fixed radar velocity and pulse repetition frequency [17], [18]. Then, both MIMO and MCSAR can be regarded as a spatial sampling process with periodically occurring errors due to the periodic evaluation of the channels. An almost equivalent sampling process is conducted by time-interleaved analog-to-digital converters (ADCs), where M ADCs with identical sampling rates are combined in a time-interleaving architecture to one ADC with M times the sampling rate [37], based on the theory of the generalized sampling expansion [3], [38]. Here, amplitude, timing, and further mismatches of the sub-ADCs lead to deterministic spurious signals, which are equivalent to the discussed ghost targets in radar images. For time-interleaved ADCs, these effects are very well analyzed and documented, e.g. in [39], [40]. The applicable findings will be applied and extended in this paper to analyze the impact of different calibration errors on MCSAR imaging. Thereby, the creation of calibration error caused ghost targets as in Fig. 1(d) will be explained thoroughly. A closed form solution will be given to predict the number and the position of occurring ghost targets in the case of calibration errors, without requiring any knowledge about the type of errors. Furthermore, for known errors, a relation for the height of the ghost targets will be derived. Based on this, we will provide rules for the worst-case distortion level in the case of unknown but bounded errors. To validate these theoretic findings in a realistic scenario, measurements using a 76 GHz FMCW MIMO radar are shown, illustrating the predicted effects and, thereby, demonstrating the good applicability of the derived relations.

The remainder of this paper is organized as follows: The considered error types of antenna arrays are modeled in Section II. The derivation of the erroneous SIMO-SAR signal model including extensions for MIMO-SAR and MIMO radar is shown in Section III. Section IV discusses the impact of a resampling step for non-uniform sampling on the error propagation. Based on the previous findings, boundaries for the worst-case signal-to-distortion ratios assuming different error types are derived in Section V. Section VI comprises a summary and discusses implications for future research. Finally, measurements are shown to validate the findings in Section VII, followed by a conclusion.

Notation: Continuous signals are written as $f(t)$, whereas discrete signals are written as $f[n] = f(nT)$. Vectors and matrices are written in bold lower and upper case letters, respectively. The nth entry of a vector $\boldsymbol{x}$ is given by $\boldsymbol{x}[n]$. The transpose of a vector or matrix is given by $(\cdot)^{\mathrm{T}}$ and the inverse of a quadratic matrix by $(\cdot)^{-1}$. $a_{\langle b \rangle}$ denotes the modulo operation a modulo b, and $\otimes$ denotes the operator of the Kronecker product. $\delta(x)$ denotes the Dirac delta function. The mean-value calculation is expressed by the operator $\bar{\cdot}$. $\angle(\cdot)$ calculates the angle of a complex number. Finally, $\lceil \cdot \rceil$ and $\lfloor \cdot \rfloor$ denote the ceiling and floor function, respectively.

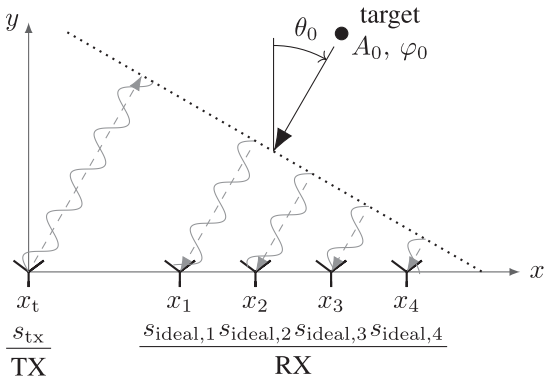

FIGURE 2. Ideal SIMO radar imaging concept comprising 4 RX antennas and a target located in the far-field under the angle θ_0.

II. CALIBRATION ERROR MODELS

In this section, different calibration errors will be described and their respective transfer function will be formulated. In this work, we limit the discussion to the linear phase and amplitude errors, phase center displacement and mutual coupling. To establish the signal model, a SIMO radar, comprising N_{r} RX antennas is assumed with its RX antennas located along the x-axis at the positions $x_{n_{\mathrm{r}}}$, $n_{\mathrm{r}} \in [1, N_{\mathrm{r}}]$ and the TX at $x = 0$. This basic measurement principle is illustrated in Fig. 2. For the sake of simplicity, all derivations will be made for a continuous wave (CW) radar emitting a transmit signal

$$s_{\mathrm{tx}}(t) = \cos(2\pi f_{\mathrm{c}} t), \tag{1}$$

with the carrier frequency f_{c}. Nevertheless, the general findings within this paper can be easily applied to common radar types, such as the FMCW radar. This will be demonstrated in Section VII, where the findings within this work are validated using a 76 GHz FMCW MIMO radar.

The transmit signal $s_{\mathrm{tx}}(t)$ is reflected at a target and received by the n_{r}th RX antenna with a delay τ_{r}, which depends on the target and antenna position. Generally, the received signal will be evaluated at the carrier frequency f_{c}. Thus, the ideally received frequency domain signal of the n_{r}th antenna can be written as

$$S_{\mathrm{ideal},n_{\mathrm{r}}}(f_{\mathrm{c}}) = A_0 \mathrm{e}^{\mathrm{j}\varphi_0} \mathrm{e}^{-\mathrm{j}2\pi f_{\mathrm{c}} \tau_{\mathrm{r}}(x_{n_{\mathrm{r}}})}, \tag{2}$$

where φ_0 introduces an additional phase shift caused by the target reflection and A_0 includes the path attenuation and the attenuation caused by the reflection at the target.

Next, $\tau_{\mathrm{r}}(x_{n_{\mathrm{r}}})$ is expressed as a continuous function $\tau_{\mathrm{r}}(x)$ along the x-axis, which is evaluated at the location of the active antenna to obtain

$$S_{\mathrm{ideal},n_{\mathrm{r}}}(f_{\mathrm{c}}) = A_0 \mathrm{e}^{\mathrm{j}\varphi_0} \mathrm{e}^{-\mathrm{j}2\pi f_{\mathrm{c}} \tau_{\mathrm{r}}(x)} \delta(x - x_{n_{\mathrm{r}}}). \tag{3}$$

Then, the phase change over the aperture can be used to define a spatial angular frequency

$$k(x) = \frac{\mathrm{d}}{\mathrm{d}x}(-2\pi f_{\mathrm{c}} \tau_{\mathrm{r}}(x)). \tag{4}$$

In the following, the standard far-field assumption will be used. Thereby, the impinging signal is described by

an incident angle θ_0 and has a constant spatial frequency $k(x) = -k_0$. Here, k_0 is defined as

$$k_0 = \frac{2\pi}{\lambda_c} \sin\theta_0, \tag{5}$$

with the carrier wavelength $\lambda_c = \frac{c_0}{f_c}$, where c_0 denotes the speed of light. $k(x) = -k_0$ was chosen to establish a positive spatial frequency for the positive angle θ_0 in Fig. 2. A received signal caused by multiple targets in the far-field is created by superposition.

In the presence of errors, the received signal can be stated as

$$S_{n_r}(f_c) = H_{\text{error},n_r}(k_0, f_c) S_{\text{ideal},n_r}(f_c), \tag{6}$$

where the channel-specific error transfer function H_{error,n_r} may depend partly on the spatial angular frequency and will be split up further in the following to represent the different error sources. First, phase errors are considered, which represent the dominating error source of antenna arrays. This is caused by the use of small wavelengths, which are necessary to enable a high measurement sensitivity of the overall system but result in large errors even for small differences in the length of the waveguides. Generally, the phase error depends on the frequency but it reduces to a constant phase φ_{n_r} per channel for the fixed frequency $f = f_c$, such that it can be modeled as

$$H_{\text{p},n_r}(f_c) = \mathrm{e}^{\mathrm{j}\varphi_{n_r}}. \tag{7}$$

Since, in most cases, relative phases are evaluated in radar imaging, only phase mismatches influence the imaging process, whereas absolute phase errors can be ignored. Hence, we can further assume without loss of generality that

$$\sum_{n_r=1}^{N_r} \varphi_{n_r} = 0. \tag{8}$$

Second, amplitude errors are caused by differences of the antenna elements' gain and the attenuation within the channel processing chain. The channel gains at f_c will be modeled with a fixed amplitude A_{n_r} per channel as

$$H_{\text{a},n_r}(f_c) = A_{n_r}. \tag{9}$$

Again, only amplitude mismatches are relevant for the reconstruction.

As a third error type, mutual coupling will be modeled. Mutual coupling at RX arrays occurs when an impinging signal is reflected at one antenna n_r' and then received at another antenna n_r. Further coupling is caused by the leakage between the transmission lines within the radar electronics. To describe the impact of the n_r'th antenna's signal onto the n_rth antenna's, a transfer function $h_{n_r,n_r'}$ is introduced, which models this specific coupling path as

$$h_{n_r,n_r'}(t) = c'_{n_r,n_r'} \delta(t - \tau_{n_r,n_r'}), \tag{10}$$

with a delay $\tau_{n_r,n_r'}$ and an attenuation factor $c'_{n_r,n_r'}$. In (10), it is assumed that the first reflection between the antennas dominates coupling since multiple reflections will lead to negligible signal amplitudes. This model for mutual coupling is typically used in band-limited systems for a simplified discussion [24]. In the frequency domain at f_c, the coupling transfer function is then given as

$$\begin{aligned} H_{n_r,n_r'}(f_c) &= c'_{n_r,n_r'} \mathrm{e}^{-\mathrm{j}2\pi f_c \tau_{n_r,n_r'}} \\ &= c_{n_r,n_r'}, \end{aligned} \tag{11}$$

where the constant phase shift introduced by the delay at a fixed frequency is included in the adapted, now complex, coupling factor $c_{n_r,n_r'}$, where $c_{n_r,n_r} = 1$ holds. Then, applying (11) to write the mutual coupling impaired receive signal (6) as

$$S_{n_r}(f_c) = \sum_{n_r'=1}^{N_r} c_{n_r,n_r'} S_{\text{ideal},n_r'}(f_c), \tag{12}$$

allows to express mutual coupling using the familiar matrix notation

$$\boldsymbol{S}(f_c) = \boldsymbol{C}\boldsymbol{S}_{\text{ideal}}(f_c), \tag{13}$$

with the coupling matrix $\boldsymbol{C}$, whose entries are given by $c_{n_r,n_r'}$, the true receive signal vector $\boldsymbol{S}(f_c) = (S_1(f_c), \ldots, S_{N_r}(f_c))^{\mathrm{T}}$ and the equivalently formed ideal receive signal vector $\boldsymbol{S}_{\text{ideal}}(f_c)$. Note that here exclusively, the vectors $\boldsymbol{S}(f_c)$ and $\boldsymbol{S}_{\text{ideal}}(f_c)$ are written as upper case bold letters, not following the notation introduced in Section I, because they denote signals in the frequency domain.

Finally, to model the influence of displaced phase centers, we define an ideal 2D antenna position as $\boldsymbol{p}_{n_r} = (x_{n_r}, 0)$ and a displaced true phase center position $\boldsymbol{p}'_{n_r} = (x_{n_r} + e_{x_{n_r}}, e_{y_{n_r}})$. The transfer function then depends on the incident angle and follows as

$$H_{\text{d},n_r}(k_0, f_c) = \mathrm{e}^{-\mathrm{j}\frac{2\pi}{\lambda_c}\Delta d_{n_r}(\theta_0)}, \tag{14}$$

with the distance difference caused by the displacement

$$\Delta d_{n_r}(\theta_0) = \sqrt{e_{x_{n_r}}^2 \sin^2\theta_0 + e_{y_{n_r}}^2 \cos^2\theta_0}. \tag{15}$$

For the combination of the discussed error types, they are assumed to occur in the order phase center displacement, mutual coupling, phase, and amplitude error. Hence, for an impinging wave with k_0, (6) can be stated with the individual error transfer functions as

$$\begin{aligned} &S_{n_r}(f_c) \\ &= H_{\text{a},n_r}(f_c) H_{\text{p},n_r}(f_c) \\ &\quad \cdot \sum_{n_r'=1}^{N_r} H_{n_r,n_r'}(f_c) H_{\text{d},n_r'}(k_0, f_c) S_{\text{ideal},n_r'}(f_c) \\ &= A_{n_r} \mathrm{e}^{\mathrm{j}\varphi_{n_r}} \sum_{n_r'=1}^{N_r} c_{n_r,n_r'} \mathrm{e}^{-\mathrm{j}\frac{2\pi}{\lambda_c}\Delta d_{n_r'}(\theta_0)} \mathrm{e}^{\mathrm{j}k_0 x_{n_r'}} \\ &= A_{n_r} \mathrm{e}^{\mathrm{j}\varphi_{n_r}} \sum_{n_r'=1}^{N_r} c_{n_r,n_r'} \mathrm{e}^{-\mathrm{j}\frac{2\pi}{\lambda_c}\Delta d_{n_r'}(\theta_0)} \mathrm{e}^{\mathrm{j}k_0 (x_{n_r} + \Delta x_{n_r'})} \end{aligned}$$

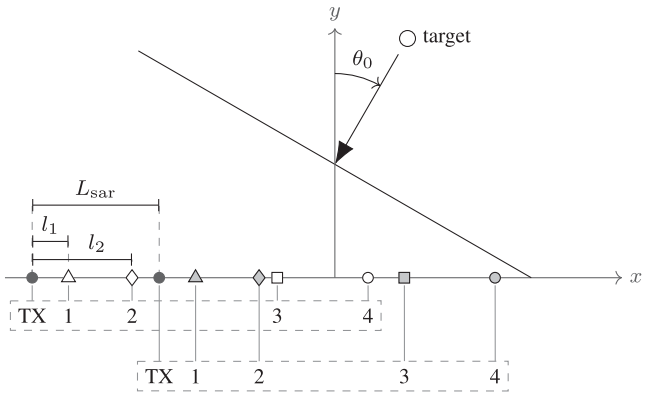

FIGURE 3. MCSAR measurement principle with a setup comprising an $N_r = 4$ element antenna array and a far-field target under the angle θ_0.

$$= \left(A_{n_r} e^{j\varphi_{n_r}} \sum_{n_{r'}=1}^{N_r} c_{n_r,n'_r} e^{j(k_0 \Delta x_{n'_r} - \frac{2\pi}{\lambda_c} \Delta d_{n'_r}(\theta_0))} \right) e^{jk_0 x_{n_r}}$$

$$= \alpha_{n_r}(k_0) e^{jk_0 x_{n_r}}$$

$$= \alpha_{n_r}(k_0) S_{n_r,\mathrm{ideal}}(f_c), \tag{16}$$

with the distance $\Delta x_{n'_r} = x_{n'_r} - x_{n_r}$ between the n'_rth and the n_rth antenna. (16) shows that for a fixed spatial frequency k_0 the influence of all error types can be expressed by a single constant complex error factor $\alpha_{n_r}(k_0)$ per antenna. Furthermore, note that phase and amplitude errors form a constant error factor independent of the spatial frequencies.

We will limit our discussion to amplitude, phase, and coupling errors for the remainder of this paper. However, the impact of phase center displacement is closely related to mutual coupling because both cause a spatial frequency dependent phase shift and can be incorporated into $\alpha_{n_r}(k_0)$, as shown above.

III. SIGNAL MODEL FOR ERRONEOUS MCSAR

This section will first derive the signal model for an erroneous SIMO-SAR. The extension to MIMO and MIMO-SAR will be presented later in the section. The basic MCSAR measurement principle is depicted in Fig. 3 for a SIMO-SAR. To derive the signal model of SIMO-SAR with calibration errors, the following assumptions are made: First, the radar is moved along the x-axis with constant speed to create the synthetic aperture. We will assume that the synthetic aperture is extended infinitely for mathematical simplicity. Measurements are taken with a distance of L_{sar}, hence, at the mth measurement point, the TX antenna is located at $x_t = (m-1)L_{\mathrm{sar}}$ and the n_rth RX antenna is located at $x_{n_r} = x_t + l_{n_r}$, where l_{n_r} denotes the constant distance between the n_rth RX and the TX antenna, see Fig. 3. Second, as before, the target is assumed to be located in the far-field with an incident angle θ_0, so (5) holds, and all derivations will be made using k_0. Note that an infinitely long synthetic aperture contradicts the far-field assumption but simplifies the subsequent derivation. All relations found in this work are also valid if only a few measurements are performed or the far-field condition is not fully met, as will be demonstrated by the simulations within this section and the measurements in Section VII. Third, the transmit signal $S_t(f)$ is assumed to have a limited bandwidth such that (13) and, thus, (16) holds [25], which should be valid for most radar systems.

A. DERIVATION OF THE SIGNAL MODEL

The received signal of the n_rth antenna with calibration errors expressed by the error factor $\alpha_{n_r}(k_0)$ is formulated generally as a continuous function of the TX position along the aperture as

$$S(x_t, f) = \alpha_{n_r}(k_0) H_{n_r}(x_t) H_t(x_t) S_t(f). \tag{17}$$

Here, the RX and TX transfer functions $H_{n_r}(x_t)$ and $H_t(x_t)$ are given by

$$H_{n_r}(x_t) = e^{jk_0(x_t + l_{n_r})} \tag{18}$$

$$H_t(x_t) = e^{jk_0 x_t}, \tag{19}$$

and describe the impact of the time delay caused by the path between the target and the RX and TX antenna, respectively. Additional constant phase and attenuation factors were discarded for simplicity. Because the evaluation of the received signal along the aperture is usually performed at fixed evaluation frequencies, the form of the band-limited transmit signal $S_t(f)$ does not influence further discussions and will be discarded in the following. Hence, all derivations will be made solely using the transfer functions, which fully contain the measured information of interest. The SAR measurement can then be modeled as a spatial sampling process with the spatial angular sampling frequency $k_s = \frac{2\pi}{L_{\mathrm{sar}}}$, yielding the sampled continuous signal as

$$y_{s,n_r}(x_t)$$

$$= \alpha_{n_r}(k_0) e^{jk_0(x_t + l_{n_r})} e^{jk_0 x_t} \sum_{m=-\infty}^{\infty} \delta(x_t - mL_{\mathrm{sar}})$$

$$= \alpha_{n_r}(k_0) \sum_{m=-\infty}^{\infty} e^{j2k_0\left(x_t + \frac{l_{n_r}}{2}\right)} \delta(x_t - mL_{\mathrm{sar}}). \tag{20}$$

In contrast to the single SIMO or MIMO case, where the TX antennas are static, both the TX and the RX antenna positions are moved during a SAR measurement, yielding the actual measured signal frequency $k_m^{\mathrm{MCSAR}} = 2k_0$. Hence, in SIMO-SAR, the incident angle θ_0 can be determined from the measured signal frequency via

$$\theta_0 = \arcsin\left(\frac{k_m^{\mathrm{MCSAR}}}{2} \frac{\lambda_c}{2\pi} \right), \tag{21}$$

which shows that an effective sampling spatial frequency of $\frac{4}{\lambda_c}$ is required to unambiguously reconstruct the angle range $\theta_0 \in [-\frac{\pi}{2}, \frac{\pi}{2}]$. Therefore, it is suitable to define equivalent antenna positions $\frac{l_{n_r}}{2}$, which allow considering the bi-static RX-TX measurements as equivalent mono-static measurements, where the sampling positions during the mth measurement

position are given by $mL_{\mathrm{sar}} + \frac{l_{n_\mathrm{r}}}{2}$ [3], [41]. Then, applying the Fourier transform (FT) along the spatial dimension x_t to (20) yields

$$Y_{\mathrm{s},n_\mathrm{r}}(\mathrm{j}k) = \frac{2\pi}{L_{\mathrm{sar}}}\alpha_{n_\mathrm{r}}(k_0)\sum_{p=-\infty}^{\infty}\delta\left(k-2k_0-p\frac{2\pi}{L_{\mathrm{sar}}}\right)\mathrm{e}^{\mathrm{j}\left(k-p\frac{2\pi}{L_{\mathrm{sar}}}\right)\frac{l_{n_\mathrm{r}}}{2}}, \tag{22}$$

with spectral replicas of the continuous spectrum with a spacing of the spatial sampling frequency $\frac{2\pi}{L_{\mathrm{sar}}}$.

Following [39], [40], all N_r receive signals are combined to get the full measurement, which according to the generalized sampling expansion will increase the effective sampling frequency to $N_\mathrm{r}\frac{2\pi}{L_{\mathrm{sar}}}$ [38]. Hence, considering (21), an unambiguous reconstruction of all frequencies resulting from $\theta_0 \in [-\frac{\pi}{2}, \frac{\pi}{2}]$ should be possible, as long as the SAR shift between two subsequent measurements is limited to

$$L_{\mathrm{sar}} \leq N_\mathrm{r}\frac{\lambda_\mathrm{c}}{4}. \tag{23}$$

To combine the signals, the discrete sampling sequences are concluded from (20) as

$$y_{\mathrm{s},n_\mathrm{r}}[m] = \alpha_{n_\mathrm{r}}(k_0)\mathrm{e}^{\mathrm{j}2k_0\left(mL_{\mathrm{sar}}+\frac{l_{n_\mathrm{r}}}{2}\right)}, \tag{24}$$

upsampled by the factor N_r, such that [39]

$$\tilde{y}_{n_\mathrm{r}}[\kappa] = \begin{cases} y_{\mathrm{s},n_\mathrm{r}}\left[\frac{\kappa}{N_\mathrm{r}}\right], & \text{if } \kappa = 0, \pm N_\mathrm{r}, \pm 2N_\mathrm{r}, \dots \\ 0 & \text{otherwise} \end{cases}, \tag{25}$$

and combined in an interleaved manner to achieve a single sequence with sampling rate $N_\mathrm{r}\frac{2\pi}{L_{\mathrm{sar}}}$, yielding

$$\tilde{y}[\kappa] = \sum_{n_\mathrm{r}=1}^{N_\mathrm{r}}\tilde{y}_{n_\mathrm{r}}[\kappa-(n_\mathrm{r}-1)]. \tag{26}$$

The FT of the combined sampled signal can then be stated using (22) as

$$\begin{aligned} Y_\mathrm{s}(\mathrm{j}k) &= \frac{1}{N_\mathrm{r}}\sum_{n_\mathrm{r}=1}^{N_\mathrm{r}}\mathrm{e}^{-\mathrm{j}k(n_\mathrm{r}-1)\frac{L_{\mathrm{sar}}}{N_\mathrm{r}}}Y_{\mathrm{s},n_\mathrm{r}}(\mathrm{j}k) \\ &= \frac{2\pi}{L_{\mathrm{sar}}}\sum_{p=-\infty}^{\infty}\sum_{n_\mathrm{r}=1}^{N_\mathrm{r}}\frac{1}{N_\mathrm{r}}\alpha_{n_\mathrm{r}}(k_0)\mathrm{e}^{\mathrm{j}\left(k-p\frac{2\pi}{L_{\mathrm{sar}}}\right)\frac{l_{n_\mathrm{r}}}{2}} \\ &\quad\cdot\mathrm{e}^{-\mathrm{j}k(n_\mathrm{r}-1)\frac{L_{\mathrm{sar}}}{N_\mathrm{r}}}\delta\left(k-2k_0-p\frac{2\pi}{L_{\mathrm{sar}}}\right). \end{aligned} \tag{27}$$

Due to arbitrary antenna positions l_{n_r} and SAR shifts L_{sar}, the combined sampling positions are non-uniform, see Fig. 3. Therefore, analogous to the signal model of time-interleaved ADCs [39], the equivalent mono-static antenna positions $\frac{l_{n_\mathrm{r}}}{2}$, introduced before, will now be expressed by the positions $(n_\mathrm{r}-1)\frac{L_{\mathrm{sar}}}{N_\mathrm{r}}$, which would yield uniform sampling in a SIMO-SAR scenario, and a deviation Δl_{n_r} from this position, such that

$$\frac{l_{n_\mathrm{r}}}{2} = (n_\mathrm{r}-1)\frac{L_{\mathrm{sar}}}{N_\mathrm{r}} - \Delta l_{n_\mathrm{r}}. \tag{28}$$

Then, the current sampling position $l_\mathrm{s}(m, n_\mathrm{r})$ of the n_rth antenna at the mth radar measurement position is given by

$$l_\mathrm{s}(m, n_\mathrm{r}) = mL_{\mathrm{sar}} + (n_\mathrm{r}-1)\frac{L_{\mathrm{sar}}}{N_\mathrm{r}} - \Delta l_{n_\mathrm{r}}. \tag{29}$$

Inserting (28) into (27) then leads to

$$\begin{aligned} Y_\mathrm{s}(\mathrm{j}k) &= \frac{2\pi}{L_{\mathrm{sar}}}\sum_{p=-\infty}^{\infty}\sum_{n_\mathrm{r}=1}^{N_\mathrm{r}}\frac{1}{N_\mathrm{r}}\alpha_{n_\mathrm{r}}(k_0)\mathrm{e}^{\mathrm{j}\left(k-p\frac{2\pi}{L_{\mathrm{sar}}}\right)\left((n_\mathrm{r}-1)\frac{L_{\mathrm{sar}}}{N_\mathrm{r}}-\Delta l_{n_\mathrm{r}}\right)} \\ &\quad\cdot\mathrm{e}^{-\mathrm{j}k(n_\mathrm{r}-1)\frac{L_{\mathrm{sar}}}{N_\mathrm{r}}}\delta\left(k-2k_0-p\frac{2\pi}{L_{\mathrm{sar}}}\right) \\ &\overset{\text{a)}}{=} \frac{2\pi}{L_{\mathrm{sar}}}\sum_{p=-\infty}^{\infty}\frac{1}{N_\mathrm{r}}\sum_{n_\mathrm{r}=1}^{N_\mathrm{r}}\alpha_{n_\mathrm{r}}(k_0)\mathrm{e}^{-\mathrm{j}2k_0\Delta l_{n_\mathrm{r}}}\mathrm{e}^{-\mathrm{j}p(n_\mathrm{r}-1)\frac{2\pi}{N_\mathrm{r}}} \\ &\quad\cdot\delta\left(k-2k_0-p\frac{2\pi}{L_{\mathrm{sar}}}\right) \\ &\overset{\text{b)}}{=} \frac{2\pi}{L_{\mathrm{sar}}}\sum_{p=-\infty}^{\infty}\beta_p\,\delta\left(k-2k_0-p\frac{2\pi}{L_{\mathrm{sar}}}\right), \end{aligned} \tag{30}$$

where at a) the sampling property of the Delta dirac function was used [42]. At b), the sum over n_r was interpreted as a discrete Fourier transform (DFT) [39], [43], showing that the spectral replicas' weighting factors β_p are given by the Fourier coefficients of the channel properties, namely $\alpha_{n_\mathrm{r}}(k_0)\mathrm{e}^{-\mathrm{j}2k_0\Delta l_{n_\mathrm{r}}}$. As a consequence of the DFT, these weighting factors are periodic so that we can state

$$\begin{aligned} \beta_p(k_0) &= \beta_{p_{\langle N_\mathrm{r}\rangle}}(k_0) \\ &= \frac{1}{N_\mathrm{r}}\sum_{n_\mathrm{r}=1}^{N_\mathrm{r}}\alpha_{n_\mathrm{r}}(k_0)\mathrm{e}^{-\mathrm{j}2k_0\Delta l_{n_\mathrm{r}}}\mathrm{e}^{-\mathrm{j}p(n_\mathrm{r}-1)\frac{2\pi}{N_\mathrm{r}}}. \end{aligned} \tag{31}$$

B. INTERPRETATION

The established relation (30) describes the combined receive spectrum of all antennas. For uniform sampling and ideal calibration, i.e. when $\Delta l_{n_\mathrm{r}} = 0$ and $\alpha_{n_\mathrm{r}} = 1$ holds for all n_r, this combined spectrum is equivalent to one caused by ideal sampling with a N_r times increased sampling frequency. Otherwise, spectral replicas of the ideal continuous receive spectrum emerge. Two main effects cause these spectral repetitions. These are the non-uniform sampling via $\mathrm{e}^{-\mathrm{j}2k_0\Delta l_{n_\mathrm{r}}}$ in (31), which is a well-known effect and discussed, e.g. in [3], and the calibration errors per channel via $\alpha_{n_\mathrm{r}}(k_0)$ in (31). Both of these effects cause peaks at the same frequencies

$$k_p = 2k_0 + p\frac{2\pi}{L_{\mathrm{sar}}}, \tag{32}$$

which are only defined by the chosen SAR shift L_{sar} and the spatial frequency k_0 caused by the true target. These

spatial frequencies k_p can directly be interpreted as incident angles θ using (21). Here, the spectral repetitions caused by non-uniform sampling generate ghost targets, when simple matched-filter-based reconstruction methods like fast FT or backprojection (BP) [31] are used. Also, inversion-based reconstruction methods, such as MUSIC and compressed sensing, are susceptible to modeling errors. They often fail due to instability or yield wrong solutions if such spectral repetitions occur. However, the effects of non-uniform sampling are generally invertible, e.g. via resampling, since the antenna geometry is usually known [3]. The effects of non-uniform sampling and this resampling step on the calibration error propagation will be discussed in the following subsection in detail.

In comparison to non-uniform sampling, the calibration errors are unknown. Hence, reconstructions cannot compensate the effects of the unknown calibration errors and, therefore, will lead to ghost targets in the final image. Naturally, the mismatches will cause N_r ghost targets within the spatial frequency band $k \in (-\frac{N_\mathrm{r}}{2L_\mathrm{sar}}, \frac{N_\mathrm{r}}{2L_\mathrm{sar}}]$. However, in radar imaging, the frequencies of interest result from the hypothetical angles $\theta \in (-\frac{\pi}{2}, \frac{\pi}{2}]$. In practice, these two intervals do not necessarily coincide, especially in automotive radar, where the driving speed influences the SAR step size. To determine the number of ghost targets in this frequency band, (32) and (21) allow us to formulate the condition

$$\left| p_\mathrm{rep} \frac{\lambda_\mathrm{c}}{2L_\mathrm{sar}} + \sin\theta_0 \right| \leq 1 \tag{33}$$

for a spectral replica with index p_rep to be located inside this interval. Hence, the relevant p_rep are given by

$$p_\mathrm{rep} \in [p_\mathrm{rep,l}, p_\mathrm{rep,u}] \cap \mathbb{Z}^*, \tag{34}$$

with $\mathbb{Z}^*$ denoting integer numbers without 0, because $p = 0$ in (30) belongs to the true target and is not considered a ghost target. The lower and upper bounds are

$$\begin{aligned} p_\mathrm{rep,l} &= \left\lceil -(1+\sin\theta_0)\frac{2L_\mathrm{sar}}{\lambda_\mathrm{c}} \right\rceil \\ p_\mathrm{rep,u} &= \left\lfloor (1-\sin\theta_0)\frac{2L_\mathrm{sar}}{\lambda_\mathrm{c}} \right\rfloor . \end{aligned} \tag{35}$$

Consequently, this leads to a total of $N_\mathrm{rep} = p_\mathrm{rep,u} - p_\mathrm{rep,l}$ ghost targets, which are located at the incident angles

$$\theta_{p_\mathrm{rep}} = \arcsin\left(\sin(\theta_0) + p_\mathrm{rep}\frac{\lambda_\mathrm{c}}{2L_\mathrm{sar}} \right) \tag{36}$$

and their amplitudes are given by $\beta_{p_\mathrm{rep}}(k_0)$ according to (31). Note that the desired target amplitude at $p = 0$ is also weighted by $\beta_0(k_0)$.

To illustrate the effects, simulations were performed assuming a SIMO-radar with $N_\mathrm{r} = 8$ RX antennas arranged as a ULA with $\frac{\lambda_\mathrm{c}}{2}$ spacing, i.e. the antennas are located at $l_{n_\mathrm{r}} = (n_\mathrm{r} - 1)\frac{\lambda_\mathrm{c}}{2}$. The same RX array will be used in the other simulations for the remainder of this work for an easy comparison. Here, the radar was moved to 64 measurement positions for a SIMO-SAR measurement with two different SAR step sizes. The resulting spectra are shown in Fig. 4. The frequency axis is exchanged by the corresponding θ-axis. For the calibration error, only phase errors were assumed, with φ_{n_r} evenly distributed in $(-\frac{\pi}{10}, \frac{\pi}{10})$. In Fig. 4(a), the SAR step size is $L_\mathrm{sar} = N_\mathrm{r}\frac{\lambda_\mathrm{c}}{4}$, leading to ideal uniform sampling. Here, the spectral replicas are solely caused by calibration errors. In Fig. 4(b), $L_\mathrm{sar} = 0.55N_\mathrm{r}\frac{\lambda_\mathrm{c}}{4}$ was chosen, which leads to oversampling of the relevant frequency interval. As a consequence, there are fewer spectral replicas visible because some spectral replicas occur at frequencies outside the reconstructed interval $\theta \in (-\frac{\pi}{2}, \frac{\pi}{2}]$. For an even stronger oversampling with $L_\mathrm{sar} \leq \frac{\lambda_\mathrm{c}}{4}$ all spectral replicas will lie outside the reconstruction interval $\theta \in (-\frac{\pi}{2}, \frac{\pi}{2}]$. This corresponds to the case where a single antenna would be sufficient to satisfy the Nyquist criterion within the SAR measurement. Furthermore, the SAR shift $L_\mathrm{sar} = 0.55N_\mathrm{r}\frac{\lambda_\mathrm{c}}{4}$ leads to non-uniform sampling, and the spectral replicas are, therefore, caused by both calibration errors and sampling errors.

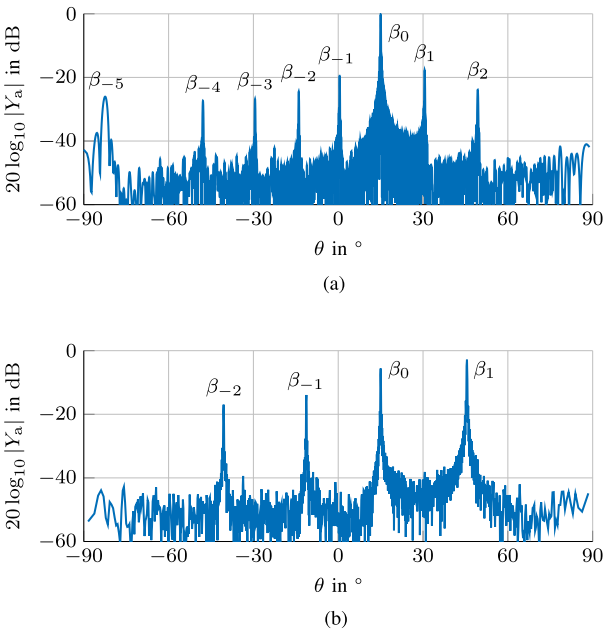

FIGURE 4. Examples of simulated receive spectra of two SIMO-SAR measurements to a single target at $\theta_0 = 15°$. An 8-element uniform RX array was assumed, which is impaired by phase calibration errors. In (a), the SAR shift was chosen to achieve uniform sampling. In (b), the SIMO-SAR aperture was sampled non-uniformly. (a) $L_\mathrm{sar} = N_\mathrm{r}\frac{\lambda_\mathrm{c}}{4}$ yielding uniform sampling. (b) $L_\mathrm{sar} = 0.55N_\mathrm{r}\frac{\lambda_\mathrm{c}}{4}$ yielding non-uniform oversampling.

C. IMPLICATIONS FOR MIMO RADAR AND MIMO-SAR

In MIMO radar, the virtual antenna array is created by the convolution of the TX array with the RX array [36]. Usually, the arrays are arranged such that one has small spacing ensuring unambiguous measurements, whereas the other is widely spaced, creating a large aperture. Without loss of generality, we assume the RX array to be closely spaced, as illustrated in Fig. 5(a). Then, a single MIMO measurement can be interpreted as an equivalent SIMO measurement with a single TX

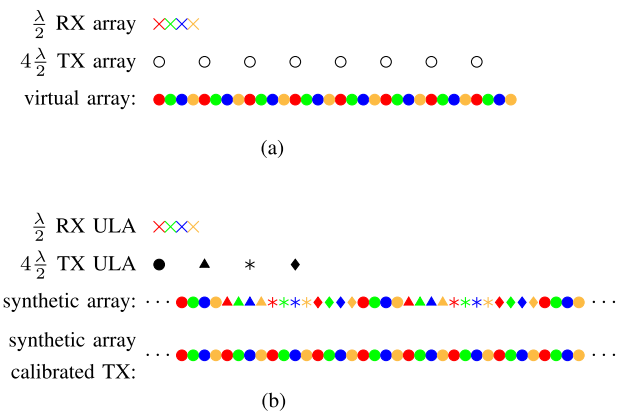

FIGURE 5. Illustration of the effective error patterns occurring during the sampling process in MIMO radar and MIMO-SAR. Each varying color and symbol refers to a sampling point associated with a channel-specific RX and TX error factor, respectively. (a) Single MIMO measurement, assuming a calibrated TX array. (b) MIMO-SAR measurement with $L_{\text{sar}}^{\text{MIMO}} = N_{\text{r}} N_{\text{t}} \frac{\lambda_{\text{c}}}{4}$.

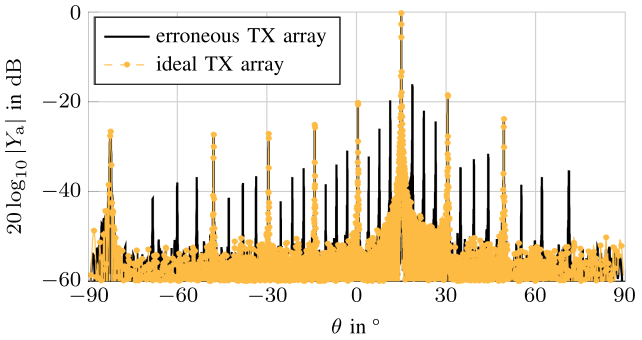

FIGURE 6. Example of a receive spectrum of a MIMO-SAR measurement to a single target at $\theta_0 = 15°$ for an ideally calibrated as well as a phase error impaired TX array. The simulated radar has the same eight antenna RX ULA used in Fig. 4, which was extended by a four antenna TX ULA, such that a uniform virtual array is achieved. In both cases, the RX array is impaired by the phase calibration errors used in Fig. 4.

at the first TX's position and a $N_{\text{t}}N_{\text{r}}$ sized virtual RX array, which consists of N_{t} repetitions of the actual RX array at the TX antenna positions. A single MIMO measurement does not lead to an interpretable image if both the TX and RX array suffer from significant calibration errors. However, for TX arrays with uniform structure, channel mismatches within the RX array yield a similar error pattern structure as the discussed SIMO-SAR case whenever calibration errors within the TX array are negligible. This effect is illustrated in Fig. 5(a), which shows the error pattern within the virtual array resulting from a MIMO array with a calibrated TX array. Note that the widely spaced TX array is much easier to calibrate than the closely spaced RX array because coupling effects can be neglected; hence, the assumption of a well-calibrated TX array often is justified in practice.

Now, the same derivations as for SIMO-SAR can be made to find identical distortion effects occurring in single MIMO radar measurements. The derivation is very similar, with the only difference that for a single MIMO measurement the measured frequency is $k_{\text{m}}^{\text{MIMO}} = k_0$ instead of $k_{\text{m}}^{\text{MCSAR}} = 2k_0$ for SIMO-SAR as in (21). This is caused by the fact that the MIMO array's virtual TX antenna is stationary compared to the moved TX antenna of a SAR. However, the unambiguous spatial frequency band is also doubled and the angle can be reconstructed from the measured frequency $k_{\text{m}}^{\text{MIMO}}$ via

$$\theta_0 = \arcsin\left(k_{\text{m}}^{\text{MIMO}} \frac{\lambda_{\text{c}}}{2\pi}\right). \tag{37}$$

Therefore, the MIMO ghost targets appear at

$$\theta_{p_{\text{rep}}}^{\text{MIMO}} = \arcsin\left(\sin(\theta_0) + p_{\text{rep}} \frac{\lambda_{\text{c}}}{L_{\text{tx}}}\right). \tag{38}$$

Often, a MIMO radar is designed to yield a uniformly distributed equivalent SIMO array with $\frac{\lambda_{\text{c}}}{2}$ spacing. To do so, the RX distance is $\frac{\lambda_{\text{c}}}{2}$, whereas the TX distance is chosen as $L_{\text{tx}} = N_{\text{r}} \frac{\lambda_{\text{c}}}{2}$ to create uniform sampling at the Nyquist border. Thus, a MIMO measurement is equivalent to a SIMO-SAR measurement whenever $L_{\text{tx}} = 2L_{\text{sar}}$ holds, see (23).

Using the equivalent SIMO assumption for a MIMO radar, the extension to a MIMO-SAR measurement is also straightforward. For the general case of calibration errors on both arrays, a virtual SIMO array with $N_{\text{r}}N_{\text{t}}$ elements can be assumed, such that all previous findings for the SIMO-SAR case can be applied without any adaptions. This is verified by a simulation shown in Fig. 6. Here, the same RX ULA including the same error pattern was used as in Fig. 4. However, the RX array is now extended to a MIMO radar using a $N_{\text{t}} = 4$ element TX ULA with $L_{\text{tx}} = N_{\text{r}} \frac{\lambda_{\text{c}}}{2}$ spacing. Here, the black spectrum shows the $N_{\text{r}}N_{\text{t}}$ artifacts caused by additional phase errors on the TX array, which are evenly distributed in $(-\frac{\pi}{10}, \frac{\pi}{10})$, yielding a total of $N_{\text{t}}N_{\text{r}} = 32$ ghost targets. However, a special case occurs if again the TX is calibrated to the degree that their remaining error factors are negligible. The resulting error structure is illustrated in Fig. 5(b). For a calibrated TX array, the repetition frequency of the error factors along the synthetic aperture is increased by the factor N_{t}. Hence, only every N_{t}th artifact will be non-zero due to the DFT, which determines the artifact heights. Thereby, the error pattern of the MIMO-SAR measurement is identical to the SIMO-SAR case, as it is visible by the resulting spectrum in Fig. 6.

IV. COMPENSATION OF NON-UNIFORM SAMPLING

As discussed before, in radar imaging, typically reconstruction methods are used, which require uniformly spaced sampling points [3], [44], [45]. Therefore, first, a resampling step must be performed. Several resampling approaches were proposed in literature as in [3], [45], [46], whereas most are based on a reinterpretation of the generalized sampling expansion given in [47]. We will now discuss the resampling in a very general manner and analyze the consequences of the impact of calibration errors on the reconstructed spectrum.

For the resampling process, we reformulate the SIMO-SAR measurement process in matrix-vector notation, assuming N_{sar}

SAR measurement positions as

$$\boldsymbol{y}_{\mathrm{nu}} = \boldsymbol{C}_{\mathrm{K}} \boldsymbol{H} \boldsymbol{x}_{Y_{\mathrm{c}}}, \tag{39}$$

where $\boldsymbol{x}_{Y_{\mathrm{c}}} \in \mathbb{C}^{N_{\mathrm{sar}} N_{\mathrm{r}}}$ denotes the discrete representation of the impinging receive signal's continuous spectrum and $\boldsymbol{H} \in \mathbb{C}^{N_{\mathrm{sar}} N_{\mathrm{r}} \times N_{\mathrm{sar}} N_{\mathrm{r}}}$ denotes the ideal measurement matrix describing the sampling process as given by the RX and TX transfer functions (18) and (19), as well as the inverse discrete Fourier transform (iDFT). The diagonal block matrix $\boldsymbol{C}_{\mathrm{K}} = \boldsymbol{I}_{N_{\mathrm{sar}}} \otimes \boldsymbol{C} \in \mathbb{C}^{N_{\mathrm{sar}} N_{\mathrm{r}} \times N_{\mathrm{sar}} N_{\mathrm{r}}}$, with the identity matrix $\boldsymbol{I}_{N_{\mathrm{sar}}}$ of the dimension N_{sar}, applies the coupling matrix to all sampling points. Note that in this representation, phase and amplitude errors are assumed to be included in $\boldsymbol{C}$. Finally, $\boldsymbol{y}_{\mathrm{nu}} \in \mathbb{C}^{N_{\mathrm{sar}} N_{\mathrm{r}}}$ contains all non-uniform sampling values of all channels as given by (26). We now define a corresponding vector of the non-uniform sampling positions $\boldsymbol{l}_{\mathrm{nu}}$ for this measurement vector. In (29), the sampling positions were described by the index m of the radar position and the index n_{r} of the receive antenna. Now, the sampling positions are expressed by a single index p, such that the pth entry of $\boldsymbol{l}_{\mathrm{nu}}$ is given by

$$\begin{aligned} \boldsymbol{l}_{\mathrm{nu}}[p] &= p \frac{L_{\mathrm{sar}}}{N_{\mathrm{r}}} - \Delta l_{p_{\langle N_{\mathrm{r}} \rangle}} \\ &= p \Delta l_{\mathrm{u}} - \Delta l_{p_{\langle N_{\mathrm{r}} \rangle}}, \end{aligned} \tag{40}$$

where $\Delta l_{\mathrm{u}} = \frac{L_{\mathrm{sar}}}{N_{\mathrm{r}}}$ is the sampling point spacing, which would lead to uniform sampling with the same sampling rate and $\Delta l_{p_{\langle N_{\mathrm{r}} \rangle}}$ are the respective periodic deviations. Furthermore, we define a vector of uniform sampling positions $\boldsymbol{l}_u$, assuming the same sampling rate as in the non-uniform case, where the pth sampling position is given by

$$\boldsymbol{l}_{\mathrm{u}}[p] = p \Delta l_{\mathrm{u}}. \tag{41}$$

The goal is now to find an alternative receive signal $\boldsymbol{y}_{\mathrm{uni}}$, which contains the sampling values corresponding to the uniform sampling positions $\boldsymbol{l}_{\mathrm{u}}$. To do so, the SIMO-SAR measurement equation in (39) is reformulated as

$$\begin{aligned} \boldsymbol{y}_{\mathrm{nu}} &= \boldsymbol{C}_{\mathrm{K}} \boldsymbol{H} \boldsymbol{x}_{Y_{\mathrm{c}}} \\ &\overset{\mathrm{a)}}{=} \boldsymbol{C}_{\mathrm{K}} \boldsymbol{H}_{\mathrm{res}} \boldsymbol{H}_{\mathrm{uni}} \boldsymbol{x}_{Y_{\mathrm{c}}} \\ &\overset{\mathrm{b)}}{=} \boldsymbol{C}_{\mathrm{K}} \boldsymbol{H}_{\mathrm{res}} \boldsymbol{y}_{\mathrm{uni,ideal}}, \end{aligned} \tag{42}$$

where at a), the measurement matrix is divided into a uniform sampling matrix $\boldsymbol{H}_{\mathrm{uni}}$, which describes the sampling process at the uniform sampling positions $\boldsymbol{l}_{\mathrm{u}}$ and is essentially an iDFT matrix, thereby causing no information loss, and a resampling matrix $\boldsymbol{H}_{\mathrm{res}}$. Consequently, in b) we can define an ideal uniform receive signal $\boldsymbol{y}_{\mathrm{uni,ideal}}$ without the influence of calibration errors. This demonstrates that $\boldsymbol{H}_{\mathrm{res}}$ represents the required linear combination of uniform sampling values to form the corresponding non-uniform sampling values. During the resampling process, this transformation is reversed by taking the inverse[1] $\boldsymbol{H}_{\mathrm{res}}^{-1}$ to get the reconstructed uniform receive signal $\boldsymbol{y}_{\mathrm{uni,rec}}$ via

$$\begin{aligned} \boldsymbol{y}_{\mathrm{uni,rec}} &= \boldsymbol{H}_{\mathrm{res}}^{-1} \boldsymbol{y}_{\mathrm{nu}} \\ &= \boldsymbol{H}_{\mathrm{res}}^{-1} \boldsymbol{C}_{\mathrm{K}} \boldsymbol{H}_{\mathrm{res}} \boldsymbol{y}_{\mathrm{uni,ideal}} \\ &= \boldsymbol{C}_{\mathrm{res}} \boldsymbol{y}_{\mathrm{uni,ideal}}. \end{aligned} \tag{43}$$

For an error-free measurement, $\boldsymbol{C}_{\mathrm{res}}$ becomes an identity matrix and, hence, the uniform signal can be reconstructed perfectly. Otherwise, a comparison of (42) and (43) shows that both non-uniform sampling and calibration errors cause the measured signal to be a linear combination of ideal samples caused by uniform sampling, demonstrating an analogy of both error sources. The linear combination then causes correlations within the spectrum and, therefore, spectral replica.

To further analyze the impact of calibration errors after resampling, the matrices' structures are exploited. Since $\boldsymbol{y}_{\mathrm{uni,ideal}}$ is the result of an iDFT, it can be expanded in a cyclic manner. Recalling the periodic structure of the non-uniform sampling positions in (40) shows that $\boldsymbol{H}_{\mathrm{res}}$ is a block-circulant matrix as in [48], where each block is of the size $N_{\mathrm{r}} \times N_{\mathrm{r}}$. Since this structure is preserved under inversion [48], the same holds for $\boldsymbol{H}_{\mathrm{res}}^{-1}$. Then, $\boldsymbol{C}_{\mathrm{res}}$ in (43) is the product of a cyclic block matrix and a diagonal block matrix and, hence, also a cyclic block matrix [49]. Therefore, the measurement error caused by calibration errors has a periodic structure, even if a resampling step is performed. The pth resampled measurement value of $\boldsymbol{y}_{\mathrm{uni,rec}}$ can then be written as

$$\begin{aligned} \boldsymbol{y}_{\mathrm{uni,rec}}[p] &= \sum_{p'=1}^{N_{\mathrm{sar}} N_{\mathrm{r}}} c_{p,p'}^{\mathrm{res}} \mathrm{e}^{\mathrm{j} k_0 \boldsymbol{l}_{\mathrm{u}}[p']} \\ &= \sum_{p'=1}^{N_{\mathrm{sar}} N_{\mathrm{r}}} c_{p,p'}^{\mathrm{res}} \mathrm{e}^{\mathrm{j} k_0 (\boldsymbol{l}_{\mathrm{u}}[p'] - \boldsymbol{l}_{\mathrm{u}}[p])} \mathrm{e}^{\mathrm{j} k_0 \boldsymbol{l}_{\mathrm{u}}[p]} \\ &= \boldsymbol{y}_{\mathrm{uni,ideal}}[p] \sum_{p'=1}^{N_{\mathrm{sar}} N_{\mathrm{r}}} c_{p,p'}^{\mathrm{res}} \mathrm{e}^{\mathrm{j} k_0 (p'-p) \Delta \boldsymbol{l}_{\mathrm{u}}} \\ &= \alpha'_p(k_0) \boldsymbol{y}_{\mathrm{uni,ideal}}[p], \end{aligned} \tag{44}$$

where $c_{p,p'}^{\mathrm{res}}$ denotes the (p, p')th entry of $\boldsymbol{C}_{\mathrm{res}}$. Here, an error factor per sampling value is defined equivalently to (16). Using the periodicity of the mismatches, which were shown before, only the first N_{r} factors must be calculated because

$$\alpha'_{n_{\mathrm{r}}}(k_0) = \alpha'_{\langle p \rangle_{N_{\mathrm{r}}}}(k_0) \tag{45}$$

holds. Hence, the error factors after the resampling step again only depend on the active antenna and can therefore be used identically to $\alpha_{n_{\mathrm{r}}}(k_0)$ in the previous section. This is further illustrated by the simulation shown in Fig. 7. Here, for an

[1] In the presented derivation, all matrices are square since the sampling rate remains unchanged by the resampling process. Furthermore, $\boldsymbol{H}_{\mathrm{res}}$ will have full rank, i.e. the inverse exists, if the generalized sampling expansion is valid. This is true as long as no sampling points coincide, which is assumed to be the case. However, if sampling points coincide, the sampling rate is effectively reduced slightly, and the inverse would have to be replaced by the pseudoinverse. Finally, note that the reconstruction quality strongly depends on the eigenvalue distribution of $\boldsymbol{H}_{\mathrm{res}}$.

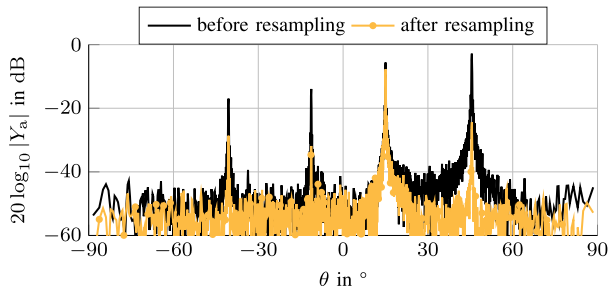

FIGURE 7. Receive spectrum of the non-uniformly sampled SIMO-SAR with phase errors, which was used in Fig. 4(b) before and after performing a resampling step to compensate the non-uniform sampling.

easy comparison, the black spectrum shows the SIMO-SAR spectrum from Fig. 4(b), which occurred for an erroneous RX array and a SAR shift of $0.55N_\mathrm{r}\frac{\lambda_\mathrm{c}}{4}$, thereby causing non-uniform sampling. The orange spectrum shows the same signal after applying a resampling step onto uniform sampling positions. While the height of the ghost targets is reduced due to the corrected sampling errors, the remaining calibration errors still cause ghost targets to appear at the predicted positions because the periodic pattern is preserved during the resampling step.

Since we have shown that non-uniformly sampled signals yield the same error structure as uniform sampling, for the sake of simplicity, in the remainder of this work, we limit all further derivations to the case of uniformly sampled signals. Consequently, $\Delta l_{n_\mathrm{r}} = 0, \forall n_\mathrm{r}$, is assumed and (31) can be simplified, yielding

$$\beta_p(k_0) = \beta_{p_{\langle N_\mathrm{r}\rangle}}(k_0) = \frac{1}{N_\mathrm{r}}\sum_{n_\mathrm{r}=1}^{N_\mathrm{r}} \alpha_{n_\mathrm{r}}(k_0)\mathrm{e}^{-\mathrm{j}p(n_\mathrm{r}-1)\frac{2\pi}{N_\mathrm{r}}}. \quad (46)$$

V. IMPACT ON SIGNAL-TO-DISTORTION RATIO

In this section, the level of distortion caused by calibration errors is analyzed by determining worst-cases for different error types. To do so, first, a signal-to-distortion ratio (SDR) is defined as

$$\begin{aligned}\mathrm{SDR}(k_0) &= 10\log_{10}\left(\frac{P_\mathrm{S}}{P_\mathrm{D}}\right)\\ &= 10\log_{10}\left(|\beta_0(k_0)|^2\right) - 10\log_{10}\left(\sum_{n_\mathrm{r}=1}^{N_\mathrm{r}-1}|\beta_{n_\mathrm{r}}(k_0)|^2\right), \quad (47)\end{aligned}$$

with the signal power P_S and the distortion error power P_D. These can be directly calculated using (46) by recalling that β_0 contains the desired signal, whereas all β_{n_r} with $p_{\langle N_\mathrm{r}\rangle} \neq 0$ contain the unwanted distortion error power. The signal and distortion power are now reformulated to find an alternative representation. First, the signal power can be expressed using $\alpha_{n_\mathrm{r}}(k_0)$ as [40]

$$\begin{aligned}P_\mathrm{S}(k_0) &= |\beta_0(k_0)|^2\\ &= \left|\frac{1}{N_\mathrm{r}}\sum_{n_\mathrm{r}=1}^{N_\mathrm{r}}\alpha_{n_\mathrm{r}}(k_0)\right|^2\\ &= \left|\frac{1}{N_\mathrm{r}}\sum_{n_\mathrm{r}=1}^{N_\mathrm{r}}\mathrm{Re}(\alpha_{n_\mathrm{r}}(k_0)) + \mathrm{j}\frac{1}{N_\mathrm{r}}\sum_{n_\mathrm{r}=1}^{N_\mathrm{r}}\mathrm{Im}(\alpha_{n_\mathrm{r}}(k_0))\right|^2\\ &\overset{\text{a)}}{=} \overline{\gamma_1}^2 + \overline{\gamma_2}^2, \quad (48)\end{aligned}$$

where at a) the definition of the absolute of a complex number was used with $|x| = \sqrt{\mathrm{Re}^2 x + \mathrm{Im}^2 x}$, and the real and imaginary parts' mean are denoted $\overline{\gamma_1}$ and $\overline{\gamma_2}$, respectively. They can also be expressed as

$$\overline{\gamma_1} = \frac{1}{N_\mathrm{r}}\sum_{n_\mathrm{r}=1}^{N_\mathrm{r}}|\alpha_{n_\mathrm{r}}(k_0)|\cos(\angle\alpha_{n_\mathrm{r}}(k_0)) \quad (49)$$

$$\overline{\gamma_2} = \frac{1}{N_\mathrm{r}}\sum_{n_\mathrm{r}=1}^{N_\mathrm{r}}|\alpha_{n_\mathrm{r}}(k_0)|\sin(\angle\alpha_{n_\mathrm{r}}(k_0)). \quad (50)$$

Second, the distortion power is given by the total power minus the power of the desired signal as

$$\begin{aligned}P_\mathrm{D}(k_0) &= \sum_{n_\mathrm{r}=1}^{N_\mathrm{r}}|\beta_{n_\mathrm{r}}(k_0)|^2 - P_\mathrm{S}(k_0)\\ &\overset{\text{a)}}{=} \frac{1}{N_\mathrm{r}}\sum_{n_\mathrm{r}=1}^{N_\mathrm{r}}|\alpha_{n_\mathrm{r}}(k_0)|^2 - P_\mathrm{S}(k_0)\\ &\overset{\text{b)}}{=} \overline{|\alpha_{n_\mathrm{r}}(k_0)|^2} - \left(\overline{\gamma_1}^2 + \overline{\gamma_2}^2\right), \quad (51)\end{aligned}$$

where at a) Parseval's theorem was used [40], and at b), the previously found alternative expression for the signal power was inserted. Hence, the SDR follows as

$$\mathrm{SDR} = 10\log_{10}\frac{\overline{\gamma_1}^2 + \overline{\gamma_2}^2}{\overline{|\alpha_{n_\mathrm{r}}(k_0)|^2} - \left(\overline{\gamma_1}^2 + \overline{\gamma_2}^2\right)}. \quad (52)$$

Next, the worst-case scenarios for different error types, namely isolated amplitude and phase errors, combined phase and amplitude errors, as well as coupling errors will be discussed. Worst-case SDRs will be derived, which allow estimating the level of distortion occurring in the radar image for a maximum expected error of the different error types. For example, large temperature differences, which lead to the circuit board's contraction or expansion, will change of the line lengths of the different channels and, thereby, cause phase errors. With the worst-case SDRs derived in the following, the expected distortion level can be calculated for a maximum expansion and, thereby, a maximum phase error. The worst-case analysis for isolated amplitude and phase errors is closely related to the one made for gain and timing mismatches of time-interleaved ADCs in [40]. Therefore, the derivation of these two cases will be rather compact. Furthermore, note that

when only amplitude and phase errors are considered, while coupling is neglected, the dependency on k_0 can be discarded.

A. AMPLITUDE ERRORS

First, only amplitude errors will be discussed. For this purpose, they are defined as $\Delta A_{n_\mathrm{r}} = A_{n_\mathrm{r}} - \overline{A_{n_\mathrm{r}}}$ with $|\Delta A_{n_\mathrm{r}}| < \overline{A_{n_\mathrm{r}}}$. Then, the error factors are given by $\alpha_{n_\mathrm{r}} = \overline{A_{n_\mathrm{r}}} + \Delta A_{n_\mathrm{r}}$, where $\overline{\Delta A_{n_\mathrm{r}}} = 0$ holds. By inserting this relation in (48) and (51), the related $\mathrm{SDR_A}$ follows as

$$\mathrm{SDR_A} = 10\log_{10}\left(\frac{\overline{A_{n_\mathrm{r}}}^2}{\overline{(\overline{A_{n_\mathrm{r}}} + \Delta A_{n_\mathrm{r}})^2} - \overline{A_{n_\mathrm{r}}}^2}\right). \tag{53}$$

To find a worst-case SDR, ΔA_{n_r} is assumed to be bounded by a maximum value $\Delta A_{\max}$ with $|\Delta A_{\max}| < \overline{A_{n_\mathrm{r}}}$. Then, [40] showed, that the worst-case SDR, indicated by the superscript wc, occurs, when all ΔA_{n_r} equal $\pm\Delta A_{\max}$. The worst-case SDR can then be simplified to

$$\mathrm{SDR_A^{wc}} = -20\log_{10}\left(\frac{\Delta A_{\max}}{\overline{A_{n_\mathrm{r}}}}\right). \tag{54}$$

B. PHASE ERRORS

The derivation of the worst-case SDR for phase errors is similar and for an extensive derivation the reader is referred to [40]. Again, phase errors are defined as $\Delta\varphi_{n_\mathrm{r}} = \varphi_{n_\mathrm{r}} - \overline{\varphi_{n_\mathrm{r}}}$, whereas we recall that $\overline{\varphi_{n_\mathrm{r}}} = 0$ holds. Then, the error factors follow as $\alpha_{n_\mathrm{r}} = \mathrm{e}^{\mathrm{j}\Delta\varphi_{n_\mathrm{r}}}$ and the SDR for only phase errors $\mathrm{SDR_P}$ can be found by inserting this in (49), (50), and (52), leading to

$$\begin{aligned}\mathrm{SDR_P} &= 10\log_{10}\frac{\overline{\gamma_1}^2 + \overline{\gamma_2}^2}{1 - \left(\overline{\gamma_1}^2 + \overline{\gamma_2}^2\right)} \\ &= -10\log_{10}\left(\frac{1}{\overline{\gamma_1}^2 + \overline{\gamma_2}^2} - 1\right) \\ &= -10\log_{10}\left(\frac{1}{\overline{\cos\Delta\varphi_{n_\mathrm{r}}}^2 + \overline{\sin\Delta\varphi_{n_\mathrm{r}}}^2} - 1\right).\end{aligned} \tag{55}$$

Again, for the worst-case scenario $\Delta\varphi_{n_\mathrm{r}}$ is assumed to be bounded by a maximum error $\Delta\varphi_{\max}$. Then, the minimum SDR can be found, by minimizing both $\overline{\cos\Delta\varphi_{n_\mathrm{r}}}^2$ and $\overline{\sin\Delta\varphi_{n_\mathrm{r}}}^2$. $\overline{\cos\Delta\varphi_{n_\mathrm{r}}}^2$ can be minimized if for all errors $|\Delta\varphi_{n_\mathrm{r}}| = \Delta\varphi_{\max}$ holds. $\overline{\sin\Delta\varphi_{n_\mathrm{r}}}^2$ is minimized to its minimal value zero, if either all $\Delta\varphi_{n_\mathrm{r}} = 0$ or the same number of errors equal plus and minus $\Delta\varphi_{\max}$, respectively, causing pairs of $\sin\Delta\varphi_{\max}$ and $\sin(-\Delta\varphi_{\max}) = -\sin\Delta\varphi_{\max}$, which add up to zero [40]. Hence, the latter yields the worst-case SDR for only phase errors, which is then given by

$$\mathrm{SDR_P^{wc}} = -10\log_{10}\left(\frac{1}{\cos^2\Delta\varphi_{\max}} - 1\right). \tag{56}$$

C. COMBINED AMPLITUDE AND PHASE ERRORS

Combined amplitude and phase errors are modeled as $\alpha_{n_\mathrm{r}} = (\overline{A_{n_\mathrm{r}}} + \Delta A_{n_\mathrm{r}})\mathrm{e}^{\mathrm{j}\Delta\varphi_{n_\mathrm{r}}}$. The SDR is then given by

$$\begin{aligned}\mathrm{SDR_{AP}} = -10\log_{10}\Bigg(&-1 \\ &+ \frac{\overline{(\overline{A_{n_\mathrm{r}}} + \Delta A_{n_\mathrm{r}})^2}}{\overline{(\overline{A_{n_\mathrm{r}}} + \Delta A_{n_\mathrm{r}})\cos\Delta\varphi_{n_\mathrm{r}}}^2 + \overline{(\overline{A_{n_\mathrm{r}}} + \Delta A_{n_\mathrm{r}})\sin\Delta\varphi_{n_\mathrm{r}}}^2}\Bigg).\end{aligned} \tag{57}$$

Finding the amplitude and phase errors, which cause a worst-case SDR in this case corresponds to finding the solution of

$$\begin{aligned}\underset{\Delta\varphi_{n_\mathrm{r}}, \Delta A_{n_\mathrm{r}}}{\operatorname{argmin}} \quad &\frac{\overline{(\overline{A_{n_\mathrm{r}}} + \Delta A_{n_\mathrm{r}})\cos\Delta\varphi_{n_\mathrm{r}}}^2}{\overline{(\overline{A_{n_\mathrm{r}}} + \Delta A_{n_\mathrm{r}})^2}} \\ &+ \frac{\overline{(\overline{A_{n_\mathrm{r}}} + \Delta A_{n_\mathrm{r}})\sin\Delta\varphi_{n_\mathrm{r}}}^2}{\overline{(\overline{A_{n_\mathrm{r}}} + \Delta A_{n_\mathrm{r}})^2}}.\end{aligned} \tag{58}$$

For now, it is assumed that, for the solution of (58), the second summand is minimized to its minimal value being zero. Then, the optimization task is reduced to

$$\underset{\Delta\varphi_{n_\mathrm{r}}, \Delta A_{n_\mathrm{r}}}{\operatorname{argmin}} \quad \frac{\overline{(\overline{A_{n_\mathrm{r}}} + \Delta A_{n_\mathrm{r}})\cos\Delta\varphi_{n_\mathrm{r}}}^2}{\overline{(\overline{A_{n_\mathrm{r}}} + \Delta A_{n_\mathrm{r}})^2}}. \tag{59}$$

Independent of the amplitude errors ΔA_{n_r}, (59) is minimized by choosing $|\Delta\varphi_{n_\mathrm{r}}| = \Delta\varphi_{\max}$, such that $\cos\Delta\varphi_{n_\mathrm{r}}$ is minimal. Then, $\cos\Delta\varphi_{n_\mathrm{r}}$ is constant and, consequently, $\overline{(\overline{A_{n_\mathrm{r}}} + \Delta A_{n_\mathrm{r}})\cos\Delta\varphi_{n_\mathrm{r}}}$ in the numerator of (59) will also be constant since $\overline{\Delta A_{n_\mathrm{r}}} = 0$ holds. This allows to further reduce (59) to

$$\underset{\Delta A_{n_\mathrm{r}}}{\operatorname{argmin}} \quad \frac{1}{\overline{(\overline{A_{n_\mathrm{r}}} + \Delta A_{n_\mathrm{r}})^2}}, \tag{60}$$

which is solved by choosing pairwise $\Delta A_{n_\mathrm{r}} = \pm\Delta A_{\max}$. The found relations $\Delta A_{n_\mathrm{r}} = \pm\Delta A_{\max}$ as well as $|\Delta\varphi_{n_\mathrm{r}}| = \Delta\varphi_{\max}$ solve (58) as long as the second part of (58) equals zero. This, in turn, can be assured by further choosing conjugate phase errors $\pm\Delta\varphi_{\max}$ for channel pairs with the same amplitude errors. Hence, by inserting $\alpha_{n_\mathrm{r}} = (\overline{A_{n_\mathrm{r}}} \pm \Delta A_{\max})\mathrm{e}^{\mathrm{j}\pm\Delta\varphi_{\max}}$ and $\alpha_{n_\mathrm{r}'} = (\overline{A_{n_\mathrm{r}}} \pm \Delta A_{\max})\mathrm{e}^{\mathrm{j}\mp\Delta\varphi_{\max}}$ in (57), the worst-case SDR for combined phase and amplitude errors is calculated as

$$\begin{aligned}&\mathrm{SDR_{AP}^{wc}} \\ &= -10\log_{10}\left(\frac{\overline{(\overline{A_{n_\mathrm{r}}} + \Delta A_{\max})^2 + (\overline{A_{n_\mathrm{r}}} - \Delta A_{\max})^2}}{\overline{A_{n_\mathrm{r}}}^2\cos^2\Delta\varphi_{\max}} - 1\right) \\ &= -10\log_{10}\left(\frac{\overline{A_{n_\mathrm{r}}}^2 + \Delta A_{\max}^2}{\overline{A_{n_\mathrm{r}}}^2\cos^2\Delta\varphi_{\max}} - 1\right).\end{aligned} \tag{61}$$

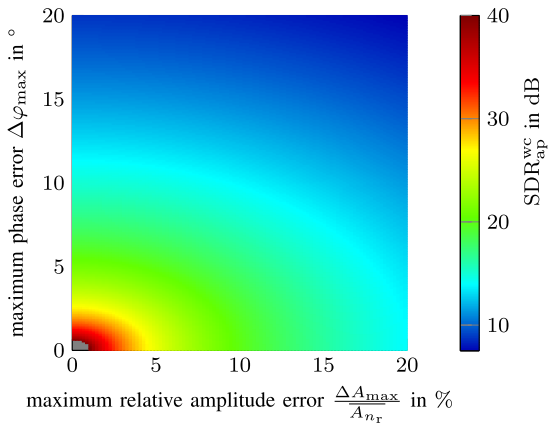

FIGURE 8. Worst-case SDRs of a 8-channel uniform array for a given combination of maximum phase errors $\Delta\varphi_{\max}$ and maximum amplitude errors $\frac{\Delta A_{\max}}{A_{n_r}}$ normed to the mean channel amplitude. Values higher than 40 dB are shown in gray.

In order to illustrate the impact of calibration errors, simulations were conducted assuming a uniform antenna array with $N_\mathrm{r} = 8$ receive channels with $\frac{\lambda_\mathrm{c}}{2}$ spacing, which, if e.g. operated at $f_\mathrm{c} = 76\,\mathrm{GHz}$, would correspond to a typical automotive radar. $L_\mathrm{sar} = N_\mathrm{r}\frac{\lambda_\mathrm{c}}{4}$ was chosen to achieve uniform sampling. Fig. 8 shows the worst-case SDRs for certain maximum values for phase and amplitude errors along the channel, demonstrating that even small errors can significantly degrade performance. For example, if only phase errors occur, the SDR is reduced by up to 20 dB for a maximum phase error of 5.7°, whereas a sole maximum relative amplitude of 10% leads to the same performance degradation. Furthermore, to verify the applicability of the worst-case SDRs as boundaries, 5000 combinations of phase and amplitude errors per channel were randomly generated within the limits defined by $\varphi_{\max} = 8°$ and $\frac{\Delta A_{\max}}{A_{n_r}} = 10\%$, respectively, for an 8 antenna RX array. This was repeated for only phase, only amplitude, and combined errors. Fig. 9 shows histograms of the according SDRs and the worst-case SDRs as dashed lines. For all simulated cases the worst-case SDRs clearly limit the occurring histograms, and the mean SDRs are approximately 5.7 dB higher in all cases. Furthermore, for combined errors, the SDR is lowered and the histogram becomes narrower because the combination of multiple random variables has an averaging effect.

D. COUPLING ERRORS

In the following, the impact of coupling errors will be discussed. For this purpose, a coupling matrix is assumed whose main diagonal equals one. All other entries, representing the actual coupling, have amplitude values that are fixed, known, and symmetric, meaning $|c_{n_\mathrm{r},n_\mathrm{r}'}| = |c_{n_\mathrm{r}',n_\mathrm{r}}|$ holds. Thereby, we account for the fact, that the coupling amplitude is mainly given by the antenna distance, and, therefore, can be assumed to be approximately known and symmetric [24]. It was discussed in [25] that the assumption of constant coupling is valid in typical radar systems with limited bandwidth such as FMCW radar. In special cases, where the above assumptions are not justified, the following derivation of a worst-case SDR may still be useful to provide a rough estimate of the expected image distortion caused by mutual coupling. The phase values of the coupling entries $c_{n_\mathrm{r},n_\mathrm{r}'}$ can take any value in $[-\pi, \pi)$, i.e. they are completely random. Furthermore, a fixed incident angle, i.e. a fixed spatial frequency k_0 is assumed. Then, the error factors $\alpha_{n_\mathrm{r}}(k_0)$ can be calculated as

$$\alpha_{n_\mathrm{r}}(k_0) = 1 + \sum_{n_\mathrm{r}'=1, n_\mathrm{r}'\neq n_\mathrm{r}}^{N_\mathrm{r}} c_{n_\mathrm{r},n_\mathrm{r}'}\mathrm{e}^{\mathrm{j}k_0\Delta x_{n_\mathrm{r}'}} \tag{62}$$

This shows, that, unlike amplitude and phase errors, calibration errors cause an additive error on $\alpha_{n_\mathrm{r}}(k_0)$. For any worst-case scenario, all error factors will have the greatest possible amplitude. This will occur, when the coupling factors $c_{n_\mathrm{r},n_\mathrm{r}'}^{\mathrm{wc}}$ are added with an identical phase during the calculation of the worst-case error factors $\alpha_{n_\mathrm{r}}^{\mathrm{wc}}(k_0)$, such that

$$\begin{aligned}
\alpha_{n_\mathrm{r}}^{\mathrm{wc}}(k_0) &= 1 + \sum_{n_\mathrm{r}'=1, n_\mathrm{r}'\neq n_\mathrm{r}}^{N_\mathrm{r}} c_{n_\mathrm{r},n_\mathrm{r}'}^{\mathrm{wc}}\mathrm{e}^{\mathrm{j}k_0\Delta x_{n_\mathrm{r}'}} \\
&= 1 + \sum_{n_\mathrm{r}'=1, n_\mathrm{r}'\neq n_\mathrm{r}}^{N_\mathrm{r}} |c_{n_\mathrm{r},n_\mathrm{r}'}|\mathrm{e}^{-\mathrm{j}k_0\Delta x_{n_\mathrm{r}'}}\mathrm{e}^{\mathrm{j}\psi_{n_\mathrm{r}}^{\mathrm{wc}}}\mathrm{e}^{\mathrm{j}k_0\Delta x_{n_\mathrm{r}'}} \\
&= 1 + \mathrm{e}^{\mathrm{j}\psi_{n_\mathrm{r}}^{\mathrm{wc}}} \sum_{n_\mathrm{r}'=1, n_\mathrm{r}'\neq n_\mathrm{r}}^{N_\mathrm{r}} |c_{n_\mathrm{r},n_\mathrm{r}'}| \\
&= 1 + \mathrm{e}^{\mathrm{j}\psi_{n_\mathrm{r}}^{\mathrm{wc}}}|c_{n_\mathrm{r}}|,
\end{aligned} \tag{63}$$

with a, yet to determine, worst-case phase per channel $\psi_{n_\mathrm{r}}^{\mathrm{wc}}$ and a fixed total coupling amplitude $|c_{n_\mathrm{r}}|$. The worst-case SDR caused by coupling $\mathrm{SDR}_{\mathrm{C}}^{\mathrm{wc}}$ is then given by (64), shown at the bottom of the next page. Note that $\mathrm{SDR}_{\mathrm{C}}^{\mathrm{wc}}$ is not a function of the spatial frequency, and, therefore, the following worst-case analysis is generally valid.

Due to the different coupling amplitudes per channel in (64), the values for $\psi_{n_\mathrm{r}}^{\mathrm{wc}}$ are difficult to find. Therefore, we will instead define an approximate $\mathrm{SDR}_{\mathrm{C,a}}^{\mathrm{wc}}$ by assuming $|c_{n_\mathrm{r}}| \approx |c|$, with a fixed value $|c|$. This approximation is mostly justified for the common case of ULAs. Then, the assumption is valid for the array's inner antennas, because coupling occurs mainly between adjacent antennas. For other antenna arrangements, this may still serve as an approximate value, which will be used here for simplification of the subsequent derivation of the worst-case SDR. Hence, $\overline{|c_{n_\mathrm{r}}|} = |c|$ allows to rearrange (64) to yield

$$\mathrm{SDR}_{\mathrm{C,a}}^{\mathrm{wc}} = \min_{\psi_{n_\mathrm{r}}^{\mathrm{wc}}} 10\log_{10}\left(\frac{\frac{1}{|c|^2} + \frac{2}{|c|}\overline{\cos\psi_{n_\mathrm{r}}^{\mathrm{wc}}} + \overline{\cos\psi_{n_\mathrm{r}}^{\mathrm{wc}}}^2 + \overline{\sin\psi_{n_\mathrm{r}}^{\mathrm{wc}}}^2}{1 - \overline{\cos\psi_{n_\mathrm{r}}^{\mathrm{wc}}}^2 - \overline{\sin\psi_{n_\mathrm{r}}^{\mathrm{wc}}}^2}\right)$$

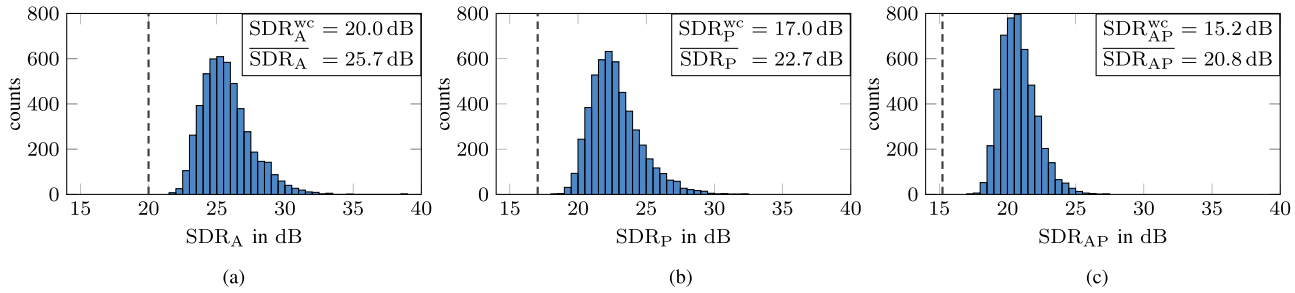

FIGURE 9. SDRs for a relative maximum amplitude error of $\frac{\Delta A_{\max}}{A_{n_{\mathrm{r}}}} = 10\%$ and a maximum phase error $\Delta\varphi_{\max} = 8°$. The dashed lines show the worst-case SDRs. The histograms show the SDRs of 5000 randomly generated phase and amplitude errors drawn from a uniform distribution between $[-\Delta\varphi_{\max}, \Delta\varphi_{\max}]$ and $[-\Delta A_{\max}, \Delta A_{\max}]$, respectively. The resulting worst-case and mean SDRs are shown in the corner. (a) Only amplitude errors. (b) Only phase errors. (c) Combined phase and amplitude errors.

$$= \min_{\psi_{n_{\mathrm{r}}}^{\mathrm{wc}}} 10\log_{10}\left(\frac{\frac{1}{|c|} + \frac{2}{|c|}\overline{\cos\psi_{n_{\mathrm{r}}}^{\mathrm{wc}}} + 1}{1 - \overline{\cos\psi_{n_{\mathrm{r}}}^{\mathrm{wc}}}^2 - \overline{\sin\psi_{n_{\mathrm{r}}}^{\mathrm{wc}}}^2} - 1\right). \tag{65}$$

As shown in the Appendix, the worst-case SDR can again be found by choosing all $\psi_{n_{\mathrm{r}}}^{\mathrm{wc}}$ to match plus/minus a, for now unknown, value ψ^{wc} and $\overline{\psi_{n_{\mathrm{r}}}^{\mathrm{wc}}} = 0$, such that (65) can be reformulated to yield

$$\mathrm{SDR}_{\mathrm{C}}^{\mathrm{wc}} = \min_{\psi^{\mathrm{wc}}} \quad 10\log_{10}\frac{\left(\frac{1}{|c|} + \cos\psi^{\mathrm{wc}}\right)^2}{1 - \cos^2\psi^{\mathrm{wc}}}, \tag{66}$$

whose derivative can be used to find analytically

$$\psi^{\mathrm{wc}} = \arccos(-|c|). \tag{67}$$

Then, the worst-case SDR for coupling errors is given by

$$\mathrm{SDR}_{\mathrm{C}}^{\mathrm{wc}} = 10\log_{10}\frac{\left(\frac{1}{|c|} + |c|\right)^2}{1 - |c|^2}, \tag{68}$$

which is shown in Fig. 10 for different values of $|c|$.

Next, a closer look is taken at the specific coupling structure of ULAs, which represent an important and often used special case of antenna arrays. Because of the uniform antenna arrangement, the coupling matrix is usually assumed to have a Toeplitz structure; hence, it is fully described by $N_{\mathrm{r}} - 1$ complex factors $c_{\mathrm{t},|n_{\mathrm{r}}-n_{\mathrm{r}}'|}$ with $n_{\mathrm{r}} \neq n_{\mathrm{r}}'$ and $\boldsymbol{C} = \mathrm{toeplitz}(1, c_{\mathrm{t},1}, \ldots, c_{\mathrm{t},N_{\mathrm{r}}-1})$. Note that in this work, a Toeplitz matrix is defined as a symmetric matrix, not a Hermitian

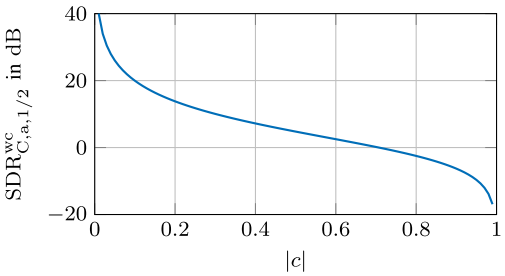

FIGURE 10. Worst-case SDR in the case of coupling for different values of the accumulated coupling amplitude.

matrix. The error factors are then given by

$$\alpha_{n_{\mathrm{r}}}(k_0) = 1 + \sum_{n_{\mathrm{r}'}=1, n_{\mathrm{r}'}\neq n_{\mathrm{r}}}^{N_{\mathrm{r}}} c_{\mathrm{t},|n_{\mathrm{r}}-n_{\mathrm{r}}'|} \mathrm{e}^{\mathrm{j}k_0\Delta x_{n_{\mathrm{r}'}}}, \tag{69}$$

and it can be seen that the above-discussed worst-cases for coupling can not occur in ULAs. In fact, for large arrays and $c_{\mathrm{t},|n_{\mathrm{r}}-n_{\mathrm{r}}'|} \to 0$ for increasing $|n_{\mathrm{r}} - n_{\mathrm{r}}'|$, all inner $\alpha_{n_{\mathrm{r}}}(k_0)$ will be identical. In this case, the distortion power caused by coupling is almost completely canceled out by the Toeplitz structure, demonstrating a favorable property of ULAs. For smaller arrays, where most $c_{\mathrm{t},|n_{\mathrm{r}}-n_{\mathrm{r}}'|}$ are greater than zero, note that within the sum in (69) the $c_{\mathrm{t},|n_{\mathrm{r}}-n_{\mathrm{r}}'|}$ has a symmetric influence along the array, whereas $\mathrm{e}^{\mathrm{j}k_0\Delta x_{n_{\mathrm{r}'}}}$ is conjugate symmetric. Recalling that the phase-only worst-case discussed above occurs when $\angle\alpha_{n_{\mathrm{r}}}$ is pairwise $\pm\Delta\varphi_{\max}$ and that $\overline{\angle\alpha_{n_{\mathrm{r}}}} = 0$ holds, shows that the worst-case SDR for Toeplitz structured coupling matrices occurs when for all coupling factors $\angle c_{\mathrm{t},|n_{\mathrm{r}}-n_{\mathrm{r}}'|} = 0$ holds and the phase error is solely introduced

$$\begin{aligned}\mathrm{SDR}_{\mathrm{C}}^{\mathrm{wc}} &= \min_{\psi_{n_{\mathrm{r}}}^{\mathrm{wc}}} \quad 10\log_{10}\left(\frac{\left(1 + \overline{|c_{n_{\mathrm{r}}}|\cos\psi_{n_{\mathrm{r}}}^{\mathrm{wc}}}\right)^2 + \overline{|c_{n_{\mathrm{r}}}|\sin\psi_{n_{\mathrm{r}}}^{\mathrm{wc}}}^2}{\left(1 + 2|c_{n_{\mathrm{r}}}|\cos\psi_{n_{\mathrm{r}}}^{\mathrm{wc}} + |c_{n_{\mathrm{r}}}|^2 - \left((1 + \overline{|c_{n_{\mathrm{r}}}|\cos\psi_{n_{\mathrm{r}}}^{\mathrm{wc}}})^2 + \overline{|c_{n_{\mathrm{r}}}|\sin\psi_{n_{\mathrm{r}}}^{\mathrm{wc}}}^2\right)\right)}\right) \\ &= \min_{\psi_{n_{\mathrm{r}}}^{\mathrm{wc}}} \quad 10\log_{10}\left(\frac{1 + 2\overline{|c_{n_{\mathrm{r}}}|\cos\psi_{n_{\mathrm{r}}}^{\mathrm{wc}}} + \overline{|c_{n_{\mathrm{r}}}|\cos\psi_{n_{\mathrm{r}}}^{\mathrm{wc}}}^2 + \overline{|c_{n_{\mathrm{r}}}|\sin\psi_{n_{\mathrm{r}}}^{\mathrm{wc}}}^2}{\overline{|c_{n_{\mathrm{r}}}|^2} - \left(\overline{|c_{n_{\mathrm{r}}}|\cos\psi_{n_{\mathrm{r}}}^{\mathrm{wc}}}^2 + \overline{|c_{n_{\mathrm{r}}}|\sin\psi_{n_{\mathrm{r}}}^{\mathrm{wc}}}^2\right)}\right).\end{aligned} \tag{64}$$

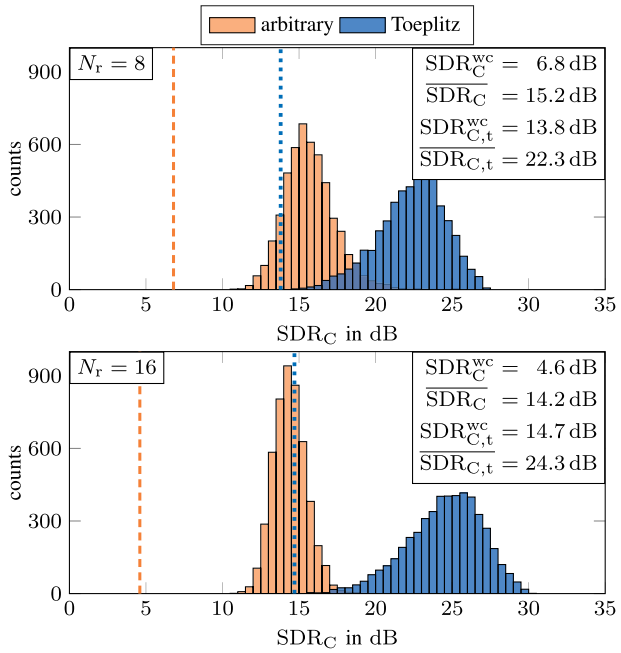

FIGURE 11. SDRs caused by coupling errors simulated by arbitrary and Toeplitz coupling matrices for an 8 (top) and a 16 (bottom) antenna ULA. The worst-case SDR for both matrix types are shown as a dashed orange (arbitrary) and dotted blue (Toeplitz) line, respectively.

by the conjugate symmetric $e^{jk_0\Delta x_{n_{r'}}}$. The corresponding SDR can then be calculated using (69) and (52).

To conclude this section, simulations were performed to illustrate the impact of coupling errors. For this purpose, the same exemplary ULA as for previous simulations was assumed. To estimate the amplitudes of the coupling matrix for this exemplary array, a field simulation of an array of 8 rectangular linear polarized patch antennas at 76 GHz with $\lambda_c/2$ distance was performed. Based on this simulation, the coupling matrix was chosen as $|\boldsymbol{C}| = \mathrm{toeplitz}(1,\ 0.12,\ 0.06,\ 0.04,\ 0.03,\ 0.02,\ 0.01,\ 0.01)$. Furthermore, a second ULA comprising $N_r = 16$ antennas was considered, where $|\boldsymbol{C}|$ was expanded by zeros, i.e. by vanishing coupling for large antenna distances. To analyze the impact of fully Toeplitz-structured coupling matrices compared to arbitrary coupling, two different simulations were performed for both array sizes. For an arbitrary coupling matrix the phases of all non-diagonal entries $\angle c_{n_r,n_r'}$ and for a Toeplitz matrix $N_r - 1$ phases $\angle c_{t,|n_r - n_r'|}$ were drawn from a uniform distribution $\mathcal{U}(-\pi, \pi]$. This was repeated 5000 times for both array sizes and both realizations forms to simulate randomly generated coupling errors. Each time the resulting SDRs were calculated. The distributions of these SDRs are shown in Fig. 11 as histograms for the 8-antenna array at the top and the 16-antenna array at the bottom. Furthermore, the worst-case SDRs are shown as dashed and dotted lines for the arbitrary and Toeplitz-shaped coupling matrices, respectively. Here, $|c| = \sum_{n_{r'}=1}^{N_r} |c_{n_r,n_r'}| - 1$ was chosen as the mean maximum coupling amplitude per channel to calculate the worst-case SDR in (68). For both the arbitrary and the Toeplitz arrays, the distance between the mean SDRs and the worst-case SDRs is approximately the same. The histograms of the arbitrary arrays are narrower because more random variables are combined, which has an averaging effect. Generally, as expected, the SDR is much higher when the Toeplitz assumption is met. Comparing the 8- and 16-antenna array shows a further increase of the Toeplitz SDR because more coupling distortion power is canceled out. For the arbitrary array, both the mean and worst-case SDR decrease when the larger array is used. This is caused by the increase in the mean coupling amplitude $|c|$ since it comprises more inner antennas, which receive high coupling power from both directions of neighboring antennas, thereby increasing the distortion power.

VI. SUMMARY OF THE FINDINGS AND IMPLICATIONS FOR FUTURE RESEARCH

In the previous sections, we analyzed the impact of calibration errors on MCSAR and MIMO systems. In these imaging systems, the signal of the receive and/or transmit array is evaluated periodically during the spatial sampling process of the incoming signal. In the case of erroneously calibrated arrays, this leads to a periodic error function on the measured signal, which then leads to repetitions of the true spectrum within the measured spectrum and causes the error power in the final image to accumulate in a few distinct ghost targets. The positions of these ghost targets are independent of the underlying calibration error type. They can be predicted only based on the true target position and knowledge about the radar movement. Furthermore, the artifacts' heights can be calculated for known errors as the periodic error function's Fourier coefficients. The respective equations are summarized in Table 1. We also proposed a simple measure for the distortion power caused by calibration errors in the form of an SDR and provided worst-case SDRs for bounded errors of different types. Again, these are summarized in Table 1.

The described effects will arise in naturally in many radar imaging applications of both MIMO and MCSAR. For example, in automotive radar, MIMO arrays are already used and SIMO-SAR raises increased interest for e.g. the search for parking spaces [20]. As another example, radar-based personnel scanners at airports use large MIMO arrays [5], where errors in individual arrays will cause the established ghost target patterns. In these safety-critical imaging applications, targets with a high dynamic range should be detectable. Often, classifying algorithms are used to find and identify target clusters as e.g. in [50], [51], [52]. However, the deterministic ghost target positions will lead to replicas of these full target clusters within the image. Hence, these repetitions will have the same characteristic features as the original target clusters and, thus, will be classified accordingly by respective algorithms. This impedes any feature-based identification of ghost targets as in [53].

This work's findings about ghost target formation may be used for automatic classifications of detections as actual

TABLE 1. Summary of the Key Equations to Predict Ghost Target Positions and Heights in MCSAR and Single MIMO Measurements, and to Estimate the SDR and Worst-Case SDRs for Different Error Types

SIMO-SAR/MIMO-SAR ($N_\mathrm{v} = N_\mathrm{r} N_\mathrm{t}$)	ghost target angles θ_{p_rep} (target at θ_0)	$\theta_{p_\mathrm{rep}} = \arcsin\left(\sin(\theta_0) + p_\mathrm{rep}\frac{\lambda_\mathrm{c}}{2L_\mathrm{sar}}\right)$ $\left\lceil -(1+\sin\theta_0)\frac{2L_\mathrm{sar}}{\lambda_\mathrm{c}}\right\rceil \le p_\mathrm{rep} \le \left\lfloor (1-\sin\theta_0)\frac{2L_\mathrm{sar}}{\lambda_\mathrm{c}}\right\rfloor$
	ghost target heights β_{p_rep} (known error factors α_{n_v})	$\beta_{p_\mathrm{rep}} = \frac{1}{N_\mathrm{v}}\sum_{n_\mathrm{v}=1}^{N_\mathrm{v}} \alpha_{n_\mathrm{v}}(k_0)\mathrm{e}^{-\mathrm{j}2k_0\Delta l_{n_\mathrm{v}}}\mathrm{e}^{-\mathrm{j}p(n_\mathrm{v}-1)\frac{2\pi}{N_\mathrm{v}}}$
single MIMO measurement (with calibrated TX array)	ghost target angles θ_{p_rep} (target at θ_0)	$\theta_{p_\mathrm{rep}} = \arcsin\left(\sin(\theta_0) + p_\mathrm{rep}\frac{\lambda_\mathrm{c}}{L_\mathrm{tx}}\right)$ $\left\lceil -(1+\sin\theta_0)\frac{L_\mathrm{sar}}{\lambda_\mathrm{c}}\right\rceil \le p_\mathrm{rep} \le \left\lfloor (1-\sin\theta_0)\frac{L_\mathrm{sar}}{\lambda_\mathrm{c}}\right\rfloor$
	ghost target heights β_{p_rep} (known error factors α_{n_r})	$\beta_{p_\mathrm{rep}} = \frac{1}{N_\mathrm{r}}\sum_{n_\mathrm{r}=1}^{N_\mathrm{r}} \alpha_{n_\mathrm{r}}(k_0)\mathrm{e}^{-\mathrm{j}k_0\Delta l_{n_\mathrm{r}}}\mathrm{e}^{-\mathrm{j}p(n_\mathrm{r}-1)\frac{2\pi}{N_\mathrm{r}}}$
SDR		$\mathrm{SDR} = 10\log_{10}\left(\lvert\beta_0(k_0)\rvert^2\right) - 10\log_{10}\left(\sum_{n_\mathrm{v}=1}^{N_\mathrm{v}-1}\lvert\beta_{n_\mathrm{v}}(k_0)\rvert^2\right)$
worst-case SDR	amplitude errors $\overline{A_{n_\mathrm{r}}} - \Delta A_\mathrm{max} \le A_{n_\mathrm{r}} \le \overline{A_{n_\mathrm{r}}} + \Delta A_\mathrm{max}$	$\mathrm{SDR}_\mathrm{A}^\mathrm{wc} = -20\log_{10}\left(\frac{\Delta A_\mathrm{max}}{\overline{A_{n_\mathrm{r}}}}\right)$
	phase errors $-\Delta\varphi_\mathrm{max} \le \Delta\varphi_{n_\mathrm{r}} \le \Delta\varphi_\mathrm{max}$	$\mathrm{SDR}_\mathrm{P}^\mathrm{wc} = -10\log_{10}\left(\frac{1}{\cos^2\Delta\varphi_\mathrm{max}} - 1\right)$
	phase and amplitude errors $\overline{A_{n_\mathrm{r}}} - \Delta A_\mathrm{max} \le A_{n_\mathrm{r}} \le \overline{A_{n_\mathrm{r}}} + \Delta A_\mathrm{max}$ $-\Delta\varphi_\mathrm{max} \le \Delta\varphi_{n_\mathrm{r}} \le \Delta\varphi_\mathrm{max}$	$\mathrm{SDR}_\mathrm{AP}^\mathrm{wc} = -10\log_{10}\left(\frac{\overline{A_{n_\mathrm{r}}}^2 + \Delta A_\mathrm{max}^2}{\overline{A_{n_\mathrm{r}}}^2\cos^2\Delta\varphi_\mathrm{max}} - 1\right)$
	coupling errors (approx. total coupling amplitude $\lvert c\rvert$)	$\mathrm{SDR}_\mathrm{C}^\mathrm{wc} = 10\log_{10}\frac{\left(\frac{1}{\lvert c\rvert}+\lvert c\rvert\right)^2}{1-\lvert c\rvert^2}$

targets or ghost targets, based on e.g. finding the characteristic artifact pattern within the image. Furthermore, it can be used to find novel metrics for the calibration quality based on the artifacts' amplitudes, thereby allowing an evaluation of the radar performance at runtime and notifying the user whether there is a need for re-calibration. Additionally, the accumulation of error power in small and known parts of the radar image may be used to establish novel calibration procedures. In conventional online calibration concepts, the unknown scattering scene usually does not allow a clear distinction of the correct and the erroneous signal, since the error power is assumed to be distributed over the full image. Using this paper's findings, artifact positions containing mainly error power can be identified. Therefore, a calibration cost function, e.g. some variation of the established SDR, can be created only based on the artifact's positions while discarding the remaining unknown image. This simplifies online-calibration in unknown environments drastically. Offline calibration approaches, as in [25], [26], already exploit the sparsity of an unknown target scene to perform simultaneous calibration and imaging. By exploiting the formation of ghost targets in a proper measurement setup, the known separation of signal and error power may significantly lower the requirements on the imaging part of such a calibration.

VII. EXPERIMENTAL VERIFICATION

In order to validate the theoretical findings within this work, measurements were performed in a realistic automotive imaging scenario. The measurement scenario is shown in Fig. 12. Here, a commercial MIMO radar using FMCW

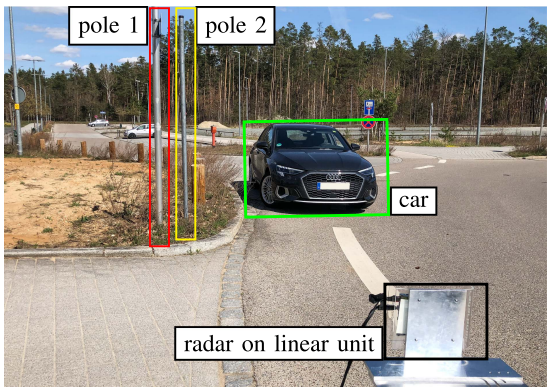

FIGURE 12. Measurement scenario used for validation of the theoretic findings with the MIMO radar mounted on a linear unit to provide the motion reference for the SAR.

measurements with a carrier frequency $f_\mathrm{c} = 76\,\mathrm{GHz}$ and a bandwidth of 1 GHz was mounted on a linear unit, which provided the motion for SAR measurements. The MIMO array consisted of $N_\mathrm{r} = 8$ element RX ULA with an antenna distance of $\frac{\lambda_\mathrm{c}}{2}$ and a $N_\mathrm{t} = 4$ element TX ULA with an antenna distance of $7\frac{\lambda_\mathrm{c}}{2}$. Since, in the case of SIMO-SAR and MIMO-SAR, the targets are partly located in the near-field of the synthetic aperture, a backprojection algorithm was used for reconstruction. The radar was calibrated using the concept proposed in [26], which provides separate coupling matrices for the TX and RX array. To validate the findings of this work, this calibration was downgraded during the reconstruction to produce calibration errors.

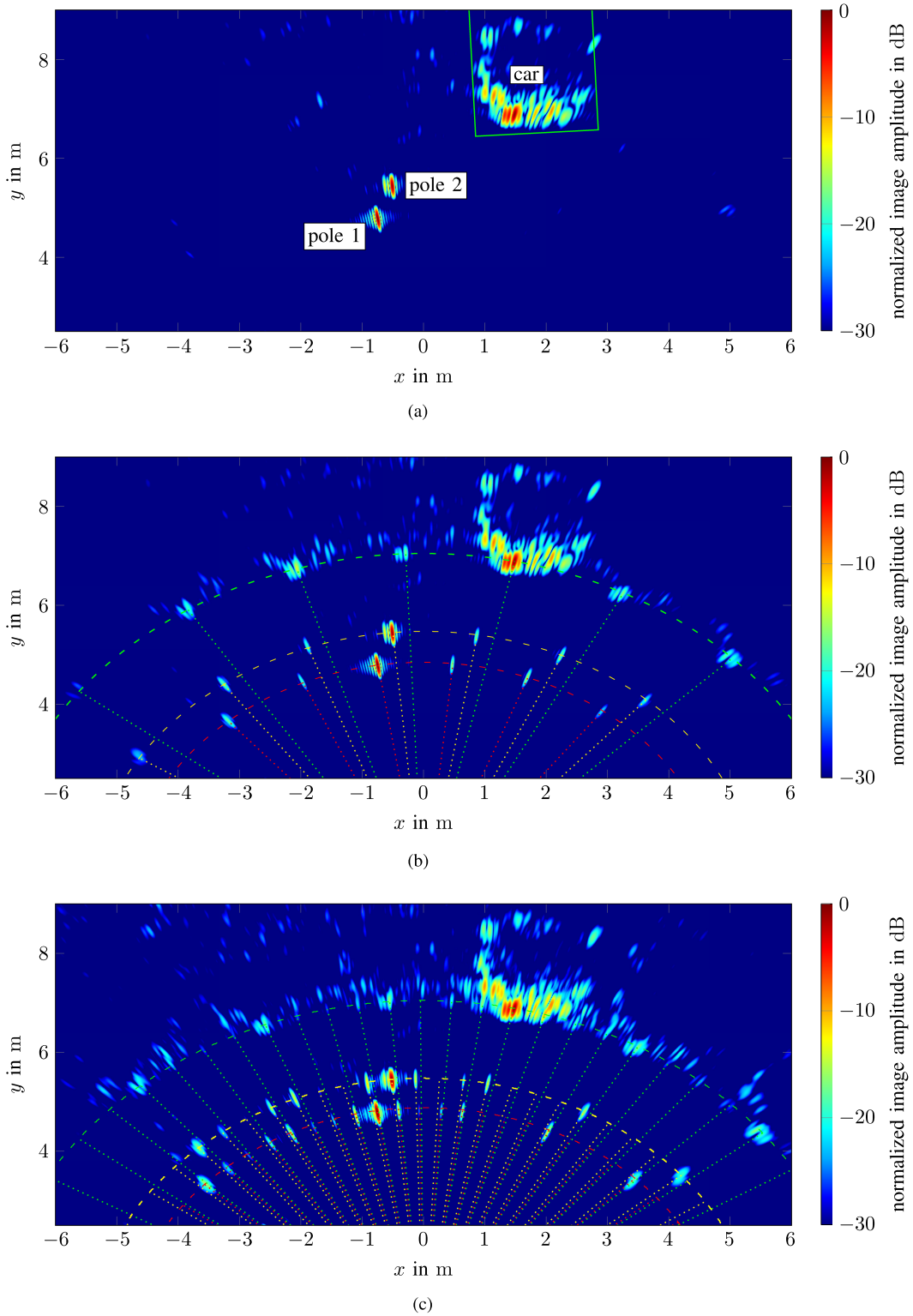

FIGURE 13. SAR images of the measurement scene in Fig. 12, reconstructed using backprojection. The dashed colored lines mark positions of equal range to the two poles and the highest reflection at the car. The colored dotted lines indicate the expected artifact angles for the two poles and the highest reflection of the car. (a) Calibrated SIMO-SAR reconstruction. (b) SIMO-SAR reconstruction with added 20° phase error. (c) MIMO-SAR reconstruction with added 20° phase error at both the RX and TX array.

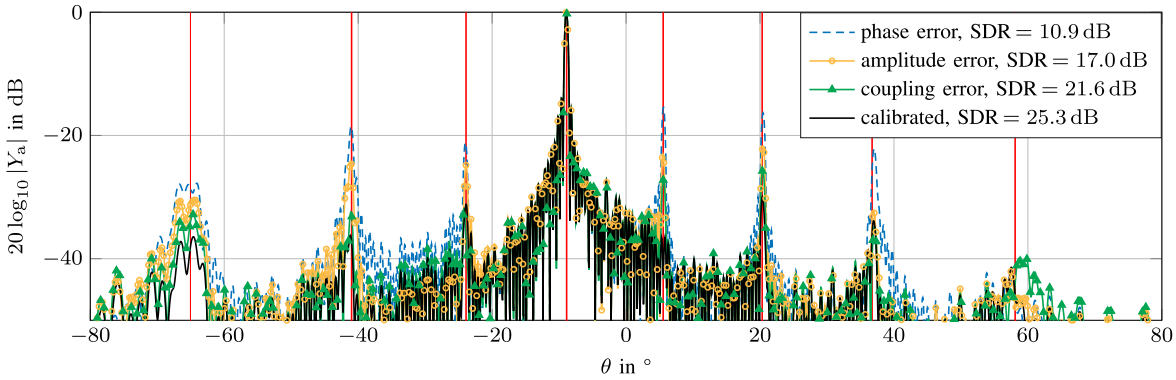

FIGURE 14. Azimuth profiles for SIMO-SAR measurement acquired by backprojection along the dashed red line through pole 1 in Fig. 13(b) for the cases that the radar is calibrated, phase error, amplitude error, and coupling error impaired. The expected ghost target positions are shown as red lines.

A. SIMO-SAR MEASUREMENT

First, a SIMO-SAR measurement was performed by moving the radar to 30 positions separated by $L_{\text{sar}} = N_{\text{r}}\frac{\lambda_{\text{c}}}{4}$, thereby creating a uniformly sampled synthetic aperture of 23 cm. For the SIMO radar measurements, only the first TX was used. The reconstructed, fully calibrated 2D-SIMO-SAR image is shown in Fig. 13(a), clearly showing the reconstructed poles and the target cluster representing the car. To downgrade the calibration, first, a 20° phase error was added to the main-diagonal entries such that for half of the antennas $\Delta\varphi_{n_{\text{r}}} = 20°$ and for the other half of the antennas $\Delta\varphi_{n_{\text{r}}} = -20°$ holds. Thereby, the worst-case condition, as discussed in Section V-B is fulfilled. The reconstructed image with additional phase errors is shown in Fig. 13(b). Here, additionally, the predicted angles based on (36) are plotted for each marked target in Fig. 12 as dotted lines as well as the arc of equal range as a dashed line. The comparison of the calibrated with the erroneous reconstruction demonstrates the deterministic formation of ghost targets due to the calibration errors, which occur at the predicted angles at the same range as the actual target. This verifies the theoretical findings in Section III. In the case of the car, Fig. 13(b) clearly illustrates how entire target clusters are repeated within the image leading to replicas of the entire car target pattern.

To further analyze the impact of different calibration errors on actual measurements, the azimuth profiles of both the calibrated and phase error impaired reconstruction along the dashed green through pole 1 are shown in Fig. 14 together with their corresponding SDRs and the expected artifact angles as red lines. An additional azimuth profile was created to demonstrate more error scenarios, where coupling errors are manually introduced by applying only the main diagonal of the RX calibration matrix during reconstruction. Furthermore, Fig. 14 also shows a reconstruction, in which a 15% amplitude error was added similarly to the phase errors before, such that for half of the array $\frac{\Delta A_{n_{\text{r}}}}{A_{n_{\text{r}}}} = 0.15$ and for the other half of the array $\frac{\Delta A_{n_{\text{r}}}}{A_{n_{\text{r}}}} = -0.15$ holds. Thereby, again, the worst-case scenario, as discussed in Section V-A, is fulfilled. The azimuth profiles show that, independent of the error type, all artifacts arise at the predicted angles. Artifacts under large angles, however, are wider and have a lower amplitude. This is caused by the violation of the far-field assumption due to the close target and large synthetic aperture in combination with the range resolution of approximately 0.15 m due to the FMCW principle.

Finally, the SDRs are analyzed. Both amplitude and phase errors were added such that they fulfill the respective worst-case SDR conditions. In case of phase errors, the resulting SDR is 10.9 dB whereas the worst-case SDR was predicted via (56) to be $\text{SDR}_{\text{P}}^{\text{wc}} = 8.8$ dB. In case of amplitude errors the measured SDR is 17.1 dB compared to a predicted worst-case SDR via (54) of $\text{SDR}_{\text{A}}^{\text{wc}} = 16.5$ dB. Hence, both measured SDRs match the expected worst-case well and only show a slightly smaller distortion. However, as discussed above, some difference is also expected since the artifacts at high angles are slightly decreased due to FMCW range resolution. Hence, this demonstrates a good agreement of the true distortion power with the predictions. Furthermore, the SDR caused by non-compensated coupling in the used ULA is 21.6 dB, which closely matches the mean value 22.3 dB for a 8-element ULA patch antenna array with a Toeplitz structured coupling matrix, which was simulated in Fig. 11 and is very similar to the radar used within the measurements. The SDR is in the expected order, thereby demonstrating both the predictions' applicability and the justification of the Toeplitz assumption.

B. MIMO-SAR AND MIMO MEASUREMENT

Second, a MIMO-SAR measurement was performed to the same scene shown in Fig. 12. Here, only $N_{\text{r}} = 7$ RX antennas were used to ensure uniform sampling during MIMO and MIMO-SAR evaluation. The radar was moved to 10 positions separated by $L_{\text{sar}}^{\text{MIMO}} = N_{\text{r}}N_{\text{t}}\frac{\lambda_{\text{c}}}{4}$, thereby creating a uniformly sampled synthetic aperture of 27 cm. To simulate calibration errors, again, ±20° phase errors were added to both the TX and RX array during the reconstruction. The resulting reconstructed image is shown in Fig. 13(c). Even though the amplitude per artifact is smaller than in the SIMO-SAR measurement, it can be seen clearly that the artifact positions

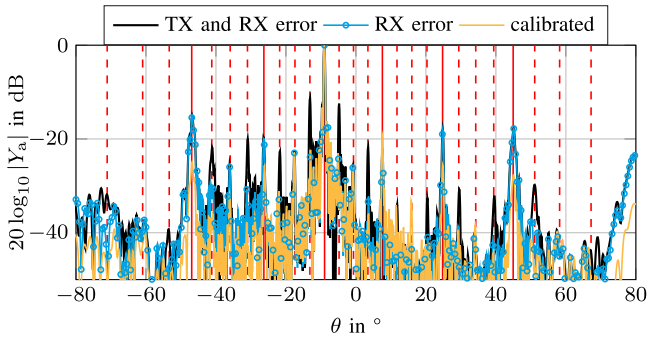

FIGURE 15. Azimuth profiles for MIMO-SAR measurement acquired by backprojection along the dashed red line through pole 1 in Fig. 13(c) for different error scenarios. In the calibrated case, the SDR is 13.6 dB, with only RX phase error 9.7 dB, and with both TX and RX phase error 5.9 dB. The expected ghost target positions mainly associated with RX errors are shown as solid red lines, whereas all other expected ghost target positions are shown as dashed red lines.

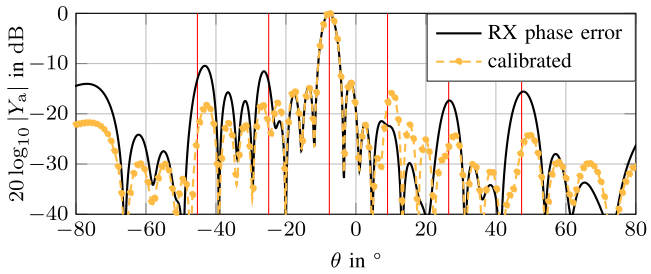

FIGURE 16. Azimuth profiles for a single MIMO measurement acquired by backprojection along the dashed red line through pole 1 in Fig. 13(c) calibrated and with phase error added to the RX array. In the calibrated case, the SDR is 8.8 dB, with RX Phase error 5.2 dB.

match the predicted positions indicated by the dotted lines. In Section III-C, we predicted that sole errors on the RX array only lead to specific artifacts. For further analysis, azimuth profiles through pole 1 were reconstructed, where the phase errors were applied to only the RX and to both the TX and RX array, respectively. The results are shown in Fig. 15, where the solid red lines show the expected artifact positions, which are mainly influenced by the RX calibration error, and the dashed red lines show the remaining artifact positions. Again, the measurements closely match the predicted behavior, further validating this work's theoretical findings.

Finally, a single MIMO measurement was performed with phase errors added to the RX array while the TX array remained calibrated. Fig. 16 shows the resulting azimuth profiles. Again, most of the distortion power caused by the calibration error is accumulated at the predicted positions, demonstrating that the discussed effects also occur within single MIMO measurements with only 4 TX antennas and, hence, 4 repetitions of the RX array.

In summary, the measurements validated the predicted formation of artifacts at the expected positions in all discussed imaging setups SIMO-SAR, MIMO, and MIMO-SAR. Also, the good applicability of the proposed worst-case SDR estimations was demonstrated. Furthermore, for MIMO-SAR, the impact of a partial calibration on the TX side on different artifacts was demonstrated. The reconstructed images of a realistic scene in Fig. 13 showed the applicability of the theoretic findings also on complex scattering clusters, which may e.g. lead to the multiple detections of the same objects or road users even within elaborated detection algorithms in automotive applications.

VIII. CONCLUSION

In this paper, it was shown that calibration errors form periodic repetitions of the spatial spectrum in all imaging systems, which repeatedly evaluate the identical array. In the radar image, this causes the error power to be accumulated at few known positions, thereby creating artifacts whose amplitudes depend on the calibration errors. Hence, it is possible to predict and recognize calibration error-induced ghost targets during the radar operation without knowing the actual calibration errors. This work derived the necessary equation tool-set to describe these effects fully and provided means to estimate the worst-case distortion level for bounded errors of different error types. Thereby, it provides the groundwork for future research enabled by the findings in this work, which should mainly focus on ghost target identification, calibration quality monitoring, and offline and online calibration.

APPENDIX

In this appendix, it is shown, that the worst-case SDR in the case of coupling errors can be found by choosing all $\psi_{n_\mathrm{r}}^{\mathrm{wc}}$ to be $\pm\psi^{\mathrm{wc}}$, while $\overline{\psi_{n_\mathrm{r}}^{\mathrm{wc}}} = 0$. Finding the worst-case corresponds to the finding the solution to the minimization problem from (65)

$$\begin{aligned}
&\min_{\psi_{n_\mathrm{r}}^{\mathrm{wc}}} \quad \frac{\frac{1}{|c|} + \frac{2}{|c|}\overline{\cos\psi_{n_\mathrm{r}}^{\mathrm{wc}}} + 1}{1 - \overline{\cos\psi_{n_\mathrm{r}}^{\mathrm{wc}}}^2 - \overline{\sin\psi_{n_\mathrm{r}}^{\mathrm{wc}}}^2} \\
&\overset{\text{a)}}{=} \min_{\psi_{n_\mathrm{r}}^{\mathrm{wc}}} \quad \frac{\frac{1}{|c|} + \frac{2}{|c|}\overline{\cos\psi_{n_\mathrm{r}}^{\mathrm{wc}}} + 1}{1 - \overline{\cos\psi_{n_\mathrm{r}}^{\mathrm{wc}}}^2 - \overline{\pm\sqrt{1-\cos\psi_{n_\mathrm{r}}^{\mathrm{wc}}}}^2},
\end{aligned} \tag{70}$$

where the identity $\cos^2 x + \sin^2 x = 1$ was used at a), while taking into account the possibly positive and negative square root. Next, we substitute $x_{n_\mathrm{r}} := \cos\psi_{n_\mathrm{r}}^{\mathrm{wc}}$, while limiting x_{n_r} to be within $[-1, 1]$. This yields the equivalent problem

$$\begin{aligned}
&\min_{x_{n_\mathrm{r}}} \quad \frac{\frac{1}{|c|} + \frac{2}{|c|}\overline{x_{n_\mathrm{r}}} + 1}{1 - \overline{x_{n_\mathrm{r}}}^2 - \overline{\pm\sqrt{1-x_{n_\mathrm{r}}^2}}^2} \\
&\text{subject to} \quad x_{n_\mathrm{r}} \in [-1, 1].
\end{aligned} \tag{71}$$

Next, assuming that $\overline{x_{n_\mathrm{r}}} = k$ holds for the solution of (71), it can be written as

$$\begin{aligned}
&\min_{x_{n_\mathrm{r}}} \quad \frac{\frac{1}{|c|} + \frac{2}{|c|}k + 1}{1 - k^2 - \overline{\pm\sqrt{1-x_{n_\mathrm{r}}^2}}^2} \\
&\text{subject to} \quad x_{n_\mathrm{r}} \in [-1, 1] \\
&\qquad\qquad \overline{x_{n_\mathrm{r}}} = k.
\end{aligned} \tag{72}$$

Since for the SDR > 0 holds, (72) can be inverted to yield the equivalent maximization problem as

$$\begin{aligned} \max_{x_{n_\mathrm{r}}} \quad & \frac{1 - k^2 - \pm\overline{\sqrt{1 - x_{n_\mathrm{r}}^2}}^2}{\frac{1}{|c|} + \frac{2}{|c|}k + 1} \\ \text{subject to} \quad & x_{n_\mathrm{r}} \in [-1, 1] \\ & \overline{x_{n_\mathrm{r}}} = k. \end{aligned} \tag{73}$$

Discarding all constant terms and negating the remaining term again leads to

$$\begin{aligned} \min_{x_{n_\mathrm{r}}} \quad & \pm\overline{\sqrt{1 - x_{n_\mathrm{r}}^2}}^2 \\ \text{subject to} \quad & x_{n_\mathrm{r}} \in [-1, 1] \\ & \overline{x_{n_\mathrm{r}}} = k. \end{aligned} \tag{74}$$

Because of its quadratic form, the minimal possible value of the objective function is zero. Now, we assume that for all n_r $x_{n_\mathrm{r}} = k$ holds. Then, (74) becomes zero by choosing pairwise the negative and positive root value, thereby providing a solution to the optimization, which does not depend on the value of k. Hence, re-substituting $x_{n_\mathrm{r}} = \cos \psi_{n_\mathrm{r}}^{\mathrm{wc}}$ shows that a worst-case solution occurs for any given k, when both $\psi_{n_\mathrm{r}}^{\mathrm{wc}} = \pm \arccos k$ and $\overline{\psi_{n_\mathrm{r}}^{\mathrm{wc}}} = 0$ hold. Finally, for a concise representation, we substitute $\psi^{\mathrm{wc}} = \arccos k$, which allows to reduce the original optimization to

$$\min_{\psi^{\mathrm{wc}}} \quad \frac{\left(\frac{1}{|c|} + \cos \psi^{\mathrm{wc}}\right)^2}{1 - \cos^2 \psi^{\mathrm{wc}}}. \tag{75}$$

REFERENCES

[1] A. Reigber et al., "Very-high-Resolution airborne synthetic aperture radar imaging: Signal processing and applications," *Proc. IEEE*, vol. 101, no. 3, pp. 759–783, Mar. 2013.

[2] A. Moreira, P. Prats-Iraola, M. Younis, G. Krieger, I. Hajnsek, and K. P. Papathanassiou, "A tutorial on synthetic aperture radar," *IEEE Geosci. Remote Sens. Mag.*, vol. 1, no. 1, pp. 6–43, Mar. 2013.

[3] G. Krieger, N. Gebert, and A. Moreira, "Unambiguous SAR signal reconstruction from nonuniform displaced phase center sampling," *IEEE Geosci. Remote Sens. Lett.*, vol. 1, no. 4, pp. 260–264, Oct. 2004.

[4] I. Ullmann, J. Adametz, D. Oppelt, A. Benedikter, and M. Vossiek, "Non-destructive testing of arbitrarily shaped refractive objects with millimetre-wave synthetic aperture radar imaging," *J. Sensors Sensor Syst.*, vol. 7, no. 1, pp. 309–317, Apr. 2018.

[5] S. S. Ahmed, A. Schiessl, F. Gumbmann, M. Tiebout, S. Methfessel, and L.-P. Schmidt, "Advanced microwave imaging," *IEEE Microw. Mag.*, vol. 13, no. 6, pp. 26–43, Sep./Oct. 2012.

[6] J. Dickmann et al., "Automotive radar the key technology for autonomous driving: From detection and ranging to environmental understanding," in *Proc. IEEE Radar Conf.*, 2016, pp. 1–6.

[7] H. Wu and T. Zwick, "Automotive SAR for parking lot detection," in *Proc. German Microw. Conf.*, 2009, pp. 1–8.

[8] C. Waldschmidt, J. Hasch, and W. Menzel, "Automotive radar from first efforts to future systems," *IEEE J. Microwaves*, vol. 1, no. 1, pp. 135–148, Jan. 2021.

[9] E. Fishler, A. Haimovich, R. Blum, D. Chizhik, L. Cimini, and R. Valenzuela, "MIMO radar: An idea whose time has come," in *Proc. IEEE Radar Conf.*, 2004, pp. 71–78.

[10] N. H. Lehmann, A. M. Haimovich, R. S. Blum, and L. Cimini, "High resolution capabilities of MIMO radar," in *Proc. IEEE 40th Asilomar Conf. Signals, Syst. Comput.*, 2006, pp. 25–30.

[11] L. Ulander, H. Hellsten, and G. Stenstrom, "Synthetic-aperture radar processing using fast factorized back-projection," *IEEE Trans. Aerosp. Electron. Syst.*, vol. 39, no. 3, pp. 760–776, Jul. 2003.

[12] T. Rommel, R. Rincon, M. Younis, G. Krieger, and A. Moreira, "Implementation of a MIMO SAR imaging mode for NASA's next generation airborne L-band SAR," in *Proc. IEEE 12th Eur. Conf. Synth. Aperture Radar*, 2018, pp. 1–5.

[13] J. H. Kim, M. Younis, P. Prats-Iraola, M. Gabele, and G. Krieger, "First spaceborne demonstration of digital beamforming for azimuth ambiguity suppression," *IEEE Trans. Geosci. Remote Sens.*, vol. 51, no. 1, pp. 579–590, Jan. 2013.

[14] N. A. Goodman, S. C. Lin, D. Rajakrishna, and J. M. Stiles, "Processing of multiple-receiver spaceborne arrays for wide-area SAR," *IEEE Trans. Geosci. Remote Sens.*, vol. 40, no. 4, pp. 841–852, Apr. 2002.

[15] T. Grebner, P. Schoeder, V. Janoudi, and C. Waldschmidt, "Radar-based mapping of the environment: Occupancy grid-map versus SAR," *IEEE Microw. Wireless Compon. Lett.*, vol. 32, no. 3, pp. 253–256, Mar. 2022.

[16] A. Laribi, M. Hahn, J. Dickmann, and C. Waldschmidt, "Performance investigation of automotive SAR imaging," in *Proc. IEEE MTT-S Int. Conf. Microw. Intell. Mobility*, 2018, pp. 1–4.

[17] R. Feger, A. Haderer, and A. Stelzer, "Experimental verification of a 77-GHz synthetic aperture radar system for automotive applications," in *Proc. IEEE MTT-S Int. Conf. Microw. Intell. Mobility*, 2017, pp. 111–114.

[18] H. Iqbal, A. Löffler, M. N. Mejdoub, and F. Gruson, "Realistic SAR implementation for automotive applications," in *Proc. 17th Eur. Radar Conf.*, 2021, pp. 306–309.

[19] X. Gao, S. Roy, and G. Xing, "MIMO-SAR: A hierarchical high-resolution imaging algorithm for mmWave FMCW radar in autonomous driving," *IEEE Trans. Veh. Technol.*, vol. 70, no. 8, pp. 7322–7334, Aug. 2021.

[20] F. Harrer, F. Pfeiffer, A. Löffler, T. Gisder, C. Buchberger, and E. Biebl, "Multi channel approaches for an automotive synthetic aperture radar," in *Proc. IEEE 11th Ger. Microw. Conf.*, 2018, pp. 391–394.

[21] C. M. Schmid, S. Schuster, R. Feger, and A. Stelzer, "On the effects of calibration errors and mutual coupling on the beam pattern of an antenna array," *IEEE Trans. Antennas Propag.*, vol. 61, no. 8, pp. 4063–4072, Aug. 2013.

[22] C. M. Schmid, C. Pfeffer, R. Feger, and A. Stelzer, "An FMCW MIMO radar calibration and mutual coupling compensation approach," in *Proc. IEEE Eur. Radar Conf.*, 2013, pp. 13–16.

[23] C. Vasanelli et al., "Calibration and direction-of-arrival estimation of millimeter-wave radars: A practical introduction," *IEEE Antennas Propag. Mag.*, vol. 62, no. 6, pp. 34–45, Dec. 2020.

[24] M. Viberg, M. Lanne, and A. Lundgren, "Calibration in array processing," in *Classical and Modern Direction-of-Arrival Estimation*. Amsterdam, The Netherlands: Elsevier, 2009, pp. 93–124.

[25] J. Geiss, E. Sippel, M. Hehn, and M. Vossiek, "Antenna array calibration using a sparse scene," *IEEE Open J. Antennas Propag.*, vol. 2, pp. 349–361, 2021.

[26] J. Geiss, E. Sippel, and M. Vossiek, "A practical concept for precise calibration of MIMO radar systems," in *Proc. IEEE 18th Eur. Radar Conf.*, 2022, pp. 405–408.

[27] C. Shipley and D. Woods, "Mutual coupling-based calibration of phased array antennas," in *Proc. IEEE Int. Conf. Phased Array Syst. Technol.*, 2000, pp. 529–532.

[28] C. Schuessler, M. Hoffmann, J. Braunig, I. Ullmann, R. Ebelt, and M. Vossiek, "A realistic radar ray tracing simulator for large MIMO-arrays in automotive environments," *IEEE J. Microwaves*, vol. 1, no. 4, pp. 962–974, Oct. 2021.

[29] M. E. Yanik and M. Torlak, "Near-field MIMO-SAR millimeter-wave imaging with sparsely sampled aperture data," *IEEE Access*, vol. 7, pp. 31801–31819, 2019.

[30] M. Shang et al., "The effects of channel imbalances on the azimuth multi-channel SAR," in *Proc. IET Int. Radar Conf.*, 2021, pp. 1561–1567.

[31] M. Soumekh, *Synthetic Aperture Radar Signal Processing*. New York, NY, USA: Wiley, 1999, vol. 7.

[32] Y. Jin, R. Prophet, A. Deligiannis, I. Weber, J.-C. Fuentes-Michel, and M. Vossiek, "Comparison of different approaches for identification of radar ghost detections in automotive scenarios," in *Proc. IEEE Radar Conf.*, 2021, pp. 1–6.

[33] F. Roos, M. Sadeghi, J. Bechter, N. Appenrodt, J. Dickmann, and C. Waldschmidt, "Ghost target identification by analysis of the Doppler distribution in automotive scenarios," in *Proc. IEEE 18th Int. Radar Symp.*, 2017, pp. 1–9.
[34] M. Murad et al., "Requirements for next generation automotive radars," in *Proc. IEEE Radar Conf.*, 2013, pp. 1–6.
[35] F. Q. de Almeida, M. Younis, G. Krieger, and A. Moreira, "An analytical error model for spaceborne SAR multichannel azimuth reconstruction," *IEEE Geosci. Remote Sens. Lett.*, vol. 15, no. 6, pp. 853–857, Jun. 2018.
[36] J. Li and P. Stoica, Eds., *MIMO Radar Signal Processing*. Hoboken, NJ, USA: Wiley, 2009.
[37] W. C. Black and D. A. Hodges, "Time interleaved converter arrays," *IEEE J. Solid-State Circuits*, vol. 15, no. 6, pp. 1022–1029, Dec. 1980.
[38] A. Papoulis, "Generalized sampling expansion," *IEEE Trans. Circuits Syst.*, vol. 24, no. 11, pp. 652–654, Nov. 1977.
[39] C. Vogel and G. Kubin, "Modeling of time-interleaved ADCs with nonlinear hybrid filter banks," *AEU - Int. J. Electron. Commun.*, vol. 59, no. 5, pp. 288–296, Jul. 2005.
[40] C. Vogel, "The impact of combined channel mismatch effects in time-interleaved ADCs," *IEEE Trans. Instrum. Meas.*, vol. 54, no. 1, pp. 415–427, Feb. 2005.
[41] N. Gebert, G. Krieger, and A. Moreira, "Digital beamforming on receive: Techniques and optimization strategies for high-resolution wide-swath SAR imaging," *IEEE Trans. Aerosp. Electron. Syst.*, vol. 45, no. 2, pp. 564–592, Apr. 2009.
[42] S. T. Karris, *Signals and Systems: With MATLAB Applications*. Fremont, California, USA: Orchard Publications, 2003.
[43] W. L. Briggs and V. E. Henson, *The DFT: An Owner's Manual for the Discrete Fourier Transform*. Philadelphia, PA, USA: SIAM, 1995.
[44] S. Chen, L. Huang, X. Qiu, M. Shang, and B. Han, "An improved imaging algorithm for high-resolution spotlight SAR with continuous PRI variation based on modified sinc interpolation," *Sensors*, vol. 19, no. 2, Jan. 2019, Art. no. 389.
[45] S. Zhao et al., "Modifications on multichannel reconstruction algorithm for SAR processing based on periodic nonuniform sampling theory and nonuniform fast fourier transform," *IEEE J. Sel. Topics Appl. Earth Observ. Remote Sens.*, vol. 8, no. 11, pp. 4998–5006, Nov. 2015.
[46] Y.-C. Jenq, "Perfect reconstruction of digital spectrum from nonuniformly sampled signals," *IEEE Trans. Instrum. Meas.*, vol. 46, no. 3, pp. 649–652, Jun. 1997.
[47] J. Brown, "Multi-channel sampling of low-pass signals," *IEEE Trans. Circuits Syst.*, vol. 28, no. 2, pp. 101–106, Feb. 1981.
[48] R. Vescovo, "Inversion of block-circulant matrices and circular array approach," *IEEE Trans. Antennas Propag.*, vol. 45, no. 10, pp. 1565–1567, Oct. 1997.
[49] I. Kra and S. R. Simanca, "On circulant matrices," *Notices Amer. Math. Soc.*, vol. 59, no. 03, pp. 368–377, Mar. 2012.
[50] E. Schubert, F. Meinl, M. Kunert, and W. Menzel, "Clustering of high resolution automotive radar detections and subsequent feature extraction for classification of road users," in *Proc. IEEE 16th Int. Radar Symp.*, 2015, pp. 174–179.
[51] R. Perez, F. Schubert, R. Rasshofer, and E. Biebl, "Single-frame vulnerable road users classification with a 77 GHz FMCW radar sensor and a convolutional neural network," in *Proc. IEEE 19th Int. Radar Symp.*, 2018, pp. 1–10.
[52] R. Prophet, M. Hoffmann, A. Ossowska, W. Malik, C. Sturm, and M. Vossiek, "Pedestrian classification for 79 GHz automotive radar systems," in *Proc. IEEE Intell. Veh. Symp. IV*, 2018, pp. 1265–1270.
[53] R. Prophet, J. Martinez, J.-C. F. Michel, R. Ebelt, I. Weber, and M. Vossiek, "Instantaneous ghost detection identification in automotive scenarios," in *Proc. IEEE Radar Conf.*, 2019, pp. 1–6.

JOHANNA GEISS (Student Member, IEEE) was born in Lich, Germany, in 1992. She received the master's degree in electrical engineering from Friedrich-Alexander-Universität Erlangen–Nürnberg, Erlangen, Germany, in 2017, where she is currently working toward the Ph.D. degree with the Institute of Microwaves and Photonics. She is primarily working on the field of radar signal processing with a focus on antenna array calibration, calibration error analysis, and SAR imaging.

ERIK SIPPEL was born in Fürth, Germany, in 1991. He received the M.Sc. and Ph.D. degrees from Friedrich-Alexander-Universität Erlangen–Nürnberg (FAU), Erlangen, Germany, in 2015 and 2022, respectively. In 2016, he joined the Institute of Microwaves and Photonics, FAU, where he is currently a Postdoctoral Researcher. His research interests include indoor localization, particularly via the evaluation of spatially distributed phase measurements, antenna array calibration for radar purposes, massive MIMO based data transmission, and time interleaved analog-to-digital conversion.

MICHAEL BRAUNWARTH was born in Augsburg, Germany, in 1993. He received the M.Sc. degree from Friedrich-Alexander-University Erlangen-Nürnberg (FAU), Erlangen, Germany, in 2019. Since 2020, he has been working toward the Ph.D. degree with the the Institute of Microwaves and Photonics, FAU. His work focuses on various aspects of radar signal processing, particularly on aspects of calibration, multiplexing schemes, and angle estimation.

MARTIN VOSSIEK (Fellow, IEEE) received the Ph.D. degree from Ruhr-Universität Bochum, Bochum, Germany, in 1996. In 1996, he joined Siemens Corporate Technology, Munich, Germany, where he was the Head of the Microwave Systems Group, from 2000 to 2003. Since 2003, he has been a Full Professor with Clausthal University, Clausthal-Zellerfeld, Germany. Since 2011, he has been the Chair of the Institute of Microwaves and Photonics (LHFT), Friedrich-Alexander-Universität Erlangen-Nürnberg (FAU), Erlangen, Germany. He has authored or coauthored more than 350 articles. His research has led to more than 100 granted patents. His research interests include radar, microwave systems, wave-based imaging, transponder, RF identification, communication, and wireless locating systems. He is a member of the German National Academy of Science and Engineering (acatech) and German Research Foundation (Dfg) Review Board. He is a member of the IEEE Microwave Theory and Technology (MTT) Technical Committees MTT-24 Microwave/mm-wave Radar, Sensing, and Array Systems, MTT-27 Connected and Autonomous Systems (as Founding Chair), MTT-29 Microwave Aerospace Systems. He is also serving on the Advisory Board of the IEEE CRFID Technical Committee on Motion Capture and Localization. He was the recipient of numerous best paper prices and other awards, and Microwave Application Award from the IEEE MTT Society (MTT-S) for Pioneering Research in Wireless Local Positioning Systems in 2019. Dr. Vossiek has been a member of organizing committees and technical program committees for many international conferences and has served on the review boards for numerous technical journals. From 2013 to 2019, he was an Associate Editor for IEEE TRANSACTIONS ON MICROWAVE THEORY AND TECHNIQUES. Since October 2022, he has been an Associate Editor-in-Chief for IEEE TRANSACTIONS ON RADAR SYSTEMS.